

# Physics-aware deep learning framework for linear elasticity

Arunabha M. Roy<sup>\*1</sup> and Rikhi Bose<sup>2</sup>

<sup>1</sup>*Aerospace Engineering, University of Michigan, Ann Arbor, MI 48109,  
U.S.A.*

<sup>2</sup>*Mechanical Engineering, Johns Hopkins University, Baltimore, MD 21218,  
U.S.A.*

## Abstract

The paper presents an efficient and robust data-driven deep learning (DL) computational framework developed for linear continuum elasticity problems. The methodology is based on the fundamentals of the Physics Informed Neural Networks (PINNs). For an accurate representation of the field variables, a multi-objective loss function is proposed. It consists of terms corresponding to the residual of the governing partial differential equations (PDE), constitutive relations derived from the governing physics, various boundary conditions, and data-driven physical knowledge fitting terms across randomly selected collocation points in the problem domain. To this end, multiple densely connected independent artificial neural networks (ANNs), each approximating a field variable, are trained to obtain accurate solutions. Several benchmark problems including the Airy solution to elasticity and the Kirchhoff-Love plate problem are solved. Performance in terms of accuracy and robustness illustrates the superiority of the current framework showing excellent agreement with analytical solutions. The present work combines the benefits of the classical methods depending on the physical information available in analytical relations with the superior capabilities of the DL techniques in the data-driven construction of lightweight, yet accurate and robust neural networks. The models developed herein can significantly boost computational speed using minimal network parameters with easy adaptability in different computational platforms.

---

<sup>\*</sup>Corresponding author — first version submitted on December, 2021

Keywords: Physics Informed Neural Networks (PINNs); Artificial neural networks (ANNs); Linear elasticity; Bi-harmonic equations; Deep learning (DL)

## 1. Introduction :

In recent years, driven by the advancement of bigdata-based architectures ([Khan et al., 2022a](#)), deep learning (DL) techniques ([LeCun et al., 2015](#)) have shown great promises in computer vision ([Voulodimos et al., 2018](#); [Roy and Bhaduri, 2021](#); [Roy et al., 2022c](#); [Roy and Bhaduri, 2022](#); [Roy et al., 2022a](#)), object detection ([Zhao et al., 2019](#); [Chandio et al., 2022](#); [Roy et al., 2022b](#); [Singh et al., 2023a](#)), image classification ([Rawat and Wang, 2017](#); [Irfan et al., 2021](#); [Jamil et al., 2022](#); [Khan et al., 2022b](#)), damage detection ([Guo et al., 2022](#); [Glowacz, 2022, 2021](#)) brain-computer interfaces ([Roy, 2022b,a,c](#); [Singh et al., 2023b](#)) and across various scientific applications ([Butler et al., 2018](#); [Ching et al., 2018](#); [Bose and Roy, 2022](#)).

The success of these methods, such as various classes of Neural Networks (NNs), can be largely attributed to their capacity in excavating large volumes of data in establishing complex high-dimensional non-linear relations between input features and output ([Kutz, 2017](#)). However, the availability of sufficient data is a major bottleneck for analyzing various complex physical systems ([Butler et al., 2018](#); [Ching et al., 2018](#)). Consequently, the majority of state-of-the-art machine learning algorithms lack robustness in predicting these systems. Upon availability of sufficient data, these have also garnered considerable success in problems governed by physics, such as dynamical systems ([Dana and Wheeler, 2020](#)), geosciences ([DeVries et al., 2018](#); [Bergen et al., 2019](#); [Racca and Magri, 2021](#); [Saha et al., 2021](#); [Jahanbakht et al., 2022](#)), material science and informatics ([Butler et al., 2018](#); [Ramprasad et al., 2017](#); [Batra et al., 2021](#); [Määttä et al., 2021](#)), fluid mechanics ([Kutz, 2017](#); [Brunton et al., 2020](#)), various constitutive modeling ([Tartakovsky et al., 2018](#); [Xu et al., 2021](#)), etc. Their applicability however may be further enhanced by utilizing physical information available by mathematical/analytical means. The recent endeavor of scientific and engineering community has been in attempting to incorporate such physical information within their predictive scheme in small data regimes.

The incorporation of physical information into the DL framework may have several advantages. First, as previously mentioned, in absence of sufficient data, it may be possible to solely utilize physical knowledge for solving such problems (Raissi et al., 2019), or to the least, enhance solutions in a data-driven predictive scheme (Raissi et al., 2020; Karniadakis et al., 2021). For example, in Sirignano and Spiliopoulos (2018), a high-dimensional Hamilton–Jacobi–Bellman PDE has been solved by approximating the solution with a DNN trained to satisfy the differential operator, initial condition, and boundary conditions. In incompressible fluid mechanics, the use of the solenoidality condition of the velocity fields restricts the solution space of the momentum equations. Therefore, this condition may be used as a constraint for solving the governing equations (conventional solvers are generally developed in a way to satisfy this constraint through the Poisson equation for pressure), or at least improve the predictions in a data-driven approach. Second, physical systems are often governed by laws that must satisfy certain properties, such as invariance under translation, rotation, reflection, etc. In a purely data-driven approach, it is almost impossible for a DL algorithm to inherit those properties entirely from data without explicit external forcing. Embedding such properties in the DL algorithm might automatically improve the accuracy of the predictions. For example, Ling et al. (2016) used a Tensor-based Neural Network (TBNN) to embed Galilean invariance that improved NN models for Reynolds-averaged Navier Stokes (RANS) simulations for the prediction of turbulent flows. And lastly, any scientific problem is governed by some underlying mechanism dictated by physical laws. Neglect of such physical information in a purely data-driven framework in the current state of affairs is, therefore, an unsophisticated approach, if not an ignorant one.

Partial differential equations (PDEs) represent underlying physical processes governed by first principles such as conservation of mass, momentum, and energy. In most cases, analytical solutions to these PDEs are not obtainable. Various numerical methods, such as finite-difference (Sengupta, 2013), finite element (FE) (Zienkiewicz and Taylor, 2005), Chebyshev and Fourier spectral methods (Boyd, 2001), etc are used to obtain approximate solutions. However, such techniques are often computationally expensive and suffer from various sources of errors due to

the complex nature of the underlying PDEs, numerical discretization and integration schemes, iterative convergence techniques, etc. Moreover, the solution of inverse problems is the current endeavor of the engineering community which requires complex formulations and is often prohibitively expensive computationally. The use of the NNs in solving/modeling the PDEs governing physical processes in a forward/ inverse problem is an important challenge worth pursuing, as these methods have the capacity to provide accurate solutions using limited computational resources in a significantly robust framework relative to the conventional methods. In this paper, we explore the possibility of using NN to obtain solutions to such PDEs governing linear continuum elasticity problems applicable in solid mechanics.

There has been a recent thrust in developing machine learning (ML) approaches to obtain the solution of governing PDEs (Karniadakis et al., 2021; von Rueden et al., 2019). The idea is to combine traditional scientific computational modeling with a data-driven ML framework to embed scientific knowledge into neural networks (NNs) to improve the performance of learning algorithms (Lagaris et al., 1998; Raissi and Karniadakis, 2018; Karniadakis et al., 2021). The *Physics Informed Neural Networks* (PINNs) (Lagaris et al., 1998; Raissi et al., 2019, 2020) were developed for the solution and discovery of nonlinear PDEs leveraging the capabilities of deep neural networks (DNNs) as universal function approximators achieving considerable success in solving forward and inverse problems in different physical problems such as fluid flows (Sun et al., 2020; Jin et al., 2021), multi-scale flows (Lou et al., 2021), heat transfer (Cai et al., 2021; Zhu et al., 2021), poroelasticity (Haghighat et al., 2022), material identification (Shukla et al., 2021), geophysics (bin Waheed et al., 2021, 2022), supersonic flows (Jagtap et al., 2022), and various other applications (Waheed et al., 2020; Bekar et al., 2022). Contrary to traditional DL approaches, PINNs force the underlying PDEs and the boundary conditions in the solution domain ensuring the correct representation of governing physics of the problem. Learning of the governing physics is ensured by the formulation of the loss function that includes the underlying PDEs; therefore labeled data to learn the mapping between inputs and outputs is no more necessary. Such architectural construction can be utilized for complex forward and inverse (finding parameters) solutions for various systems of ODEs and PDEs (Karniadakis et al., 2021). Additionally, the feed-forward neural networks utilize graph-based automated

differentiation (AD) (Baydin et al., 2018) to approximate the derivative terms in the PDEs. Various PINNs architectures notably self-adaptive PINNs (McClenny and Braga-Neto, 2020), extended PINNs (XPINN) (Hu et al., 2021; De Ryck et al., 2022) have been proposed that demonstrated superior performance. Moreover, multiple DNN-based solvers such as cPINN (Jagtap et al., 2020), XPINNs (Jagtap and Karniadakis, 2021), and PINNs framework for solid mechanics (Haghighat et al., 2021b) have been developed that provide important advancement in terms of both robustness and faster computation. In this regard, (Haghighat et al., 2020, 2021b) have been the breakthrough works geared towards developing a DL-based solver for inversion and surrogate modeling in solid mechanics for the first time utilizing PINNs theory. Additionally, PINNs have been successfully applied to the solution and discovery in linear elastic solid mechanics (Zhang et al., 2020; Samaniego et al., 2020; Haghighat et al., 2021a; Guo and Haghighat, 2020; Vahab et al., 2021; Rezaei et al., 2022; Zhang et al., 2022), elastic-viscoplastic solids (Frankel et al., 2020; Goswami et al., 2022; Arora et al., 2022; Roy and Guha, 2022), brittle fracture (Goswami et al., 2020) and computational elastodynamics (Rao et al., 2021) etc. The solution of PDEs corresponding to elasticity problems can be obtained by minimizing the network’s loss function that comprises the residual error of governing PDEs and the initial/boundary conditions. In this regard, PINNs can be utilized as a computational framework for the data-driven solution of PDE-based linear elasticity problems that can significantly boost computational speed with limited network parameters. The potential of the PINNs framework in achieving computational efficiency beyond the capacity of the conventional computational methods for solving complex problems in linear continuum elasticity is the main motivation behind the present work.

In the present work, an efficient data-driven deep learning computational framework has been presented based on the fundamentals of PINNs for the solution of the linear elasticity problem in continuum solid mechanics. In order to efficiently incorporate physical information for the elasticity problem, an improved multi-objective loss considering additional physics-constrained terms has been carefully formulated that consists of the residual of governing PDE, various boundary conditions, and data-driven physical knowledge fitting terms that demonstrate the efficacy of the model by accurately capturing the elasticity solution. Several benchmark prob-

lems including the Airy solution to an elastic plane-stress problem for an end-loaded cantilever beam and simply supported rectangular Kirchhoff-Love thin plate under transverse sinusoidal loading conditions have been solved which illustrates the superiority of the proposed model in terms of accuracy and robustness by revealing excellent agreement with analytical solutions. The employed models consist of independent multi-layer ANNs that are separately trained on minimizing the prescribed loss function specific to the problem under consideration. The performance of PINNs has been evaluated for different activation functions and network architectures. Furthermore, we have illustrated the applicability of data-driven enhancement using the smart initialization of a data-driven learning-based approach in reducing training time, while simultaneously improving the accuracy of the model which is not possible in conventional numerical algorithms. Such an approach would be important in achieving computational efficiency beyond the capacity of conventional computational methods for solving complex linear elasticity problems. The present study also demonstrates the contribution of analytical solutions for the data-driven construction of an accurate and robust PINNs framework that can significantly boost computational speed utilizing minimal trainable network parameters.

The paper is organized as follows: Section 2 introduces the background of PINNs theory and the generalized idea of implementing multi-objective loss function into the PINNs framework; In section 3, a brief overview of the theory of linear elasticity has been presented; Section 4 introduces the extension of the proposed PINNs framework for the Airy solution to an elastic plane-stress problem for an end-loaded cantilever beam; in section 5, the proposed PINNs framework has been extended to the solution of Kirchhoff–Love thin plate governed by Biharmonic PDE; Section 7 deals with the relevant finding and prospects of the current work. Finally, the conclusions have been discussed in section 8.

## **2. Physics-Informed Neural Networks :**

The concept of training a NN in the PINNs framework is the construction of the loss function. The loss function is intended to embed the underlying physics which is represented in mathematical terms by the PDEs and the associated boundary conditions. In this section, we discuss the construction of the proposed multi-object loss functions for embedding a data-driven phys-

ical model that has been associated with the PINNs framework.

Let us consider a fully connected NN defined by

$$\mathcal{N}^{k+1}(\mathcal{N}^k) = \varkappa^k(\mathbf{W}^k \cdot \mathcal{N}^k + \mathbf{b}^k) \quad (1)$$

where  $k \in \{0, 1, \dots, N\}$  represents the layer number of NN.  $\mathcal{N}$  is a nonlinear map defined by  $\mathcal{N}^m(\hat{\mathbf{x}}^m) := \varkappa^m(\mathbf{W}^m \cdot \mathbf{x}^m + \mathbf{b}^m)$  for  $m^{\text{th}}$ -layer where  $\mathbf{W}^m$  and  $\mathbf{b}^m$  represents the weights and biases of this transformation, respectively;  $\varkappa(\cdot)$  is the non-linear transformer or activation function acting on a vector element-wise. Therefore,  $k = 0$  represents the input layer of the NN taking in the input  $\mathbf{x}^0$ .

Also consider a steady state general nonlinear partial differential operator  $\mathcal{G}$  operated on a scalar solution variable  $\phi(\vec{x})$  such that,

$$\mathcal{G}\phi(\vec{x}) = 0 \quad \vec{x} \in \mathbb{R}^{n_{dim}} \quad (2)$$

Since  $\mathcal{G}$  is a differential operator, in general, Eq. 2 is accompanied by appropriate boundary conditions to ensure the existence and uniqueness of a solution. Let us assume, it is subjected to the boundary condition  $\mathcal{B}\phi(\partial\vec{\Gamma}) = \tau(\partial\vec{x})$  on the boundary  $\vec{\Gamma}$  in domain  $\Omega \in \mathbb{R}^{n_{dim}}$ ,  $n_{dim}$  being the spatial dimension. In a PINNs framework, the solution to Eq. 2,  $\phi(\mathbf{x})$ , subjected to the aforementioned boundary condition may be approximated for an input  $\mathbf{x} = \vec{x}$  by constructing a feed-forward NN expressed mathematically as

$$\hat{\phi} = \mathcal{N}^N \odot \mathcal{N}^{N-1} \odot \dots \odot \mathcal{N}^0(\mathbf{x}) \quad (3)$$

where  $\hat{\phi}$  is the approximate solution to Eq. 2;  $\odot$  denotes the general compositional construction of the NN; the input to the NN  $\mathcal{N}^0 := \mathbf{x}^0 = \vec{x} = (x_1, x_2, \dots, x_{n_{dim}})$  is the spatial coordinate at which the solution is sought. Following Eq. 1 and Eq. 3, if  $\mathbf{W}^i$  and  $\mathbf{b}^i$  are all collected in  $\theta = \bigcup_{i=0}^N(\mathbf{W}^i, \mathbf{b}^i)$ , the output layer  $\mathcal{N}^N$  contains the approximate solution  $\hat{\phi}(\vec{x})$  to the PDE such that

$$\mathcal{N}^{k+1} = \hat{\phi}[\mathbf{x}, \theta] = [\hat{\phi}_1, \hat{\phi}_2, \dots, \hat{\phi}_m] \quad (4)$$

The spatial dependence of  $\hat{\phi}$  is implicitly contained in the NN parameter  $\theta$ . In the internal/ hidden layers of NN, several variations of nonlinear transformer or the activation function  $\varkappa$  may be used, such as, the hyperbolic-tangent function  $\tanh(\xi)$ , the sigmoid function

$\varkappa(\xi) = 1/(1 + e^{-\xi})$ , the rectified linear unit (ReLU)  $\varkappa(\xi) = \max(0, \xi)$ , etc. The activation in the final layer is generally taken to be linear for regression-type problems considered here.

## 2.1 Embedding constraints in NN :

This section briefly describes the general idea of embedding linear constraints into NN (Lagaris et al., 1998; Du and Zaki, 2021). Let us consider  $\mathbb{U}$  and  $\mathbb{A}$ , two complete normed vector spaces, where NN function class  $\mathbb{M} \subset \mathbb{U}$  need to be constrained. A linear constraint on  $\phi \in \mathbb{M}$  can be expressed as:

$$\mathcal{P}\phi(\mathbf{x}) = 0, \quad \phi \in \mathbb{M} \quad (5)$$

where,  $\mathcal{P} : \mathbb{U} \rightarrow \mathbb{A}$  expresses a linear operator on  $\mathbb{U}$ . Generally, a such constraint can be realized for solving PDEs in most of the DL framework by minimizing the following functional

$$\mathcal{J}_A = \|\mathcal{P}\phi\|_{\mathbb{A}}, \quad \phi \in \mathbb{M} \quad (6)$$

where  $\|\cdot\|_{\mathbb{A}}$  denotes the norm corresponding to space  $\mathbb{A}$ . It is noteworthy to mention that the aforementioned procedure approximately enforces linear constraint in Eq. 5. However, the accuracy of the imposed constraint relies on the relative weighting between the constraint and other objectives involved in the training include the satisfaction of the governing PDEs or the integration of data-driven schemes.

## 2.2 Multiple objective loss functions :

In order to incorporate physical information of the problem, one of the possibilities is to impose Eq. 2 as a *hard constraint* in  $\mathbf{x} \in \Omega$  while training the NN on the physical data. Mathematically, such a condition is imposed by formulating a constrained optimization problem which can be expressed as (Krishnapriyan et al., 2021),

$$\min_{\theta} \Delta_{\mathcal{L}}(\mathbf{x}, \theta) \quad \text{s.t.} \quad \mathcal{G}\phi(\vec{x}) = 0. \quad (7)$$

where  $\Delta_{\mathcal{L}}$  represents data-driven physical knowledge fitting term which includes the imposed initial and boundary conditions.  $\mathcal{G}\phi(\vec{x})$  denotes the constraint corresponding to the residual



PDE imposing the governing PDE itself. Thus, it is important to carefully impose appropriate constraints for the NN to realize the underlying physics of the problem.

In the present work, we propose a multi-objective loss function that consists of residuals of governing PDEs, various boundary conditions, and data-driven physical knowledge fitting terms that can be expressed in the following general form:

$$\Delta_{\mathcal{L}}(\mathbf{x}, \theta) = \varphi \|\mathcal{G}\phi(\mathbf{x}) - \hat{0}\|_{\Omega} + \beta_u \|\mathcal{B}^{\Gamma_u}\phi - g^{\Gamma_u}\|_{\Gamma_u} + \beta_t \|\mathcal{B}^{\Gamma_t}\phi - g^{\Gamma_t}\|_{\Gamma_t} + \alpha \|\phi - \hat{\phi}\|_{\Omega} + \dots \quad (8)$$

where,  $\Delta_{\mathcal{L}}(\mathbf{x}, \theta)$  is the total loss function; the symbol  $\|\odot\|$  represents the mean squared error norm, i.e.,  $\|\odot\| = MSE(\odot)$  for regression type problem;  $\|\mathcal{G}\phi(\mathbf{x}) - \hat{0}\|_{\Omega}$  denotes the residual of the governing differential relation in Eq. 2 for  $\mathbf{x} \in \Omega$ ;  $\Gamma_u$  and  $\Gamma_t$  are the Dirichlet and Neumann boundaries subjected to conditions  $\mathcal{B}^{\Gamma_u}\phi = g^{\Gamma_u}$  and  $\mathcal{B}^{\Gamma_t}\phi = g^{\Gamma_t}$ , respectively. The values of  $g^{\Gamma_u}$  and  $g^{\Gamma_t}$  are specific to the problem under consideration, and therefore, pre-specified as inputs to the problem/ loss function. Note  $\varphi$ ,  $\beta_u$ , and,  $\beta_t$ , are weights associated with each loss term regularizing the emphasis on each term (the higher the relative value, the more emphasis on satisfying the relation). The remaining task is to utilize standard optimization techniques to tune the parameters of the NN minimizing the proposed objective/ loss function  $\Delta_{\mathcal{L}}(\mathbf{x}, \theta)$  in Eq. 8.

However, even with a large volume of training data, such an approach may not guarantee that the NN strictly obeys the conservation/governing equations in Eq. 2. Thus, additional loss terms to fit the observation data can be introduced. Hence, in the proposed objective loss function, additional loss terms such as  $\|\phi - \bar{\phi}\|_{\Omega}$  have been included that represent the data-driven physical knowledge fitting term for the state variable  $\phi(\vec{x})$ . Here,  $\bar{\phi}$  is the true (target) value of  $\phi$  provided from either the analytical solution (if available), numerical simulation, or experimental observations.  $\alpha$  is the weight associated with the data-driven physical knowledge fitting term for  $\phi(\vec{x})$ . In the NN approximation, various degrees of differentials of the state variable  $\phi(\mathbf{x})$  (i.e.,  $\phi'(\mathbf{x})$ ,  $\phi''(\mathbf{x})$ ,  $\dots$ ) can also be included (if known) for stronger coupling in the data-driven approach. The partial differentials of  $\phi(\mathbf{x})$  may be evaluated utilizing the graph-based automatic differentiation (Baydin et al., 2018) with multiple hidden layers representing the nonlinear response in PINNs. Following the same steps, the initial conditions can also be incorporated in Eq. 8. The loss from the initial conditions is not included herein due to the quasi-static nature of the elasticity problem. In a more general case, the additional loss term

$\|\phi_0 - \hat{\phi}_0\|_{\Omega}^{t=t_0}$  should be added for the loss contribution from the initial condition.

Finally, the optimal network parameters of NN  $\tilde{\theta}$  can be obtained by optimizing the loss function in Eq. 8 as

$$\tilde{\theta} = \arg \min_{\theta \in \mathbb{R}^{N^t}} \Delta_{\mathcal{L}}(\bar{\mathbf{X}}, \theta). \quad (9)$$

where,  $\tilde{\theta} := \bigcup_{i=0}^N (\tilde{\mathbf{W}}^i, \tilde{\mathbf{b}}^i)$  is the set of optimized network parameters;  $N^t$  is the total number of trainable parameters; and  $\bar{\mathbf{X}} \in \mathbb{R}^{N_c \times N^t}$  is the set of  $N_c$  collocation points used for optimization.

### 3 Theory of linear elastic solid:

Consider an undeformed configuration  $\mathcal{B}$  of an elastic body bounded in the domain  $\Omega \subset \mathbb{R}^{n_{dim}}$  ( $1 \leq n_{dim} \leq 3$ ) with boundary  $\Gamma = \Gamma_u \cup \Gamma_t$  where  $\Gamma_u \neq \emptyset$  is the Dirichlet boundary,  $\Gamma_t$  is the Neumann boundary, and  $\Gamma_u \cap \Gamma_t = \emptyset$ . With respect to the undeformed surface, the elastic body can be subjected to a prescribed displacement  $\bar{\mathbf{u}}$  on  $\Gamma_D$ , and a prescribed surface traction  $\bar{\mathbf{t}} \in [\mathcal{L}^2(\Gamma_t)]^{n_{dim}}$ . Additionally, a body force of density  $\mathbf{B} \in [\mathcal{L}^2(\Omega)]^{n_{dim}}$  in  $\Omega$  can be prescribed with respect to the undeformed volume. Using a standard basis  $\{\mathbf{e}_i\}$  in  $\mathbb{R}^{n_{dim}}$ , we can express the displacement,  $\mathbf{u} = u_i \mathbf{e}_i$ , and its gradient,  $\nabla \mathbf{u} = \frac{1}{2} (u_{i,j} + u_{j,i}) \mathbf{e}_i \otimes \mathbf{e}_j$ ; where,  $\otimes$  denotes the tensor products. Second order symmetric tensors are linear transformations in  $\mathbb{S}$ , defined as  $\mathbb{S} := \{\boldsymbol{\xi} : \mathbb{R}^{n_{dim}} \rightarrow \mathbb{R}^{n_{dim}} \mid \boldsymbol{\xi} = \boldsymbol{\xi}^T\}$  with inner product  $\boldsymbol{\xi} : \boldsymbol{\xi} = \text{tr} [\boldsymbol{\xi} \boldsymbol{\xi}^T] \equiv \xi_{ij} \xi_{ij}$ . Therefore, the stress tensor can be expressed as  $\boldsymbol{\sigma} := \sigma_{ij} \mathbf{e}_i \otimes \mathbf{e}_j$ . For infinitesimal strain, displacement gradient tensor  $\nabla \mathbf{u}$  can be expressed as:  $\nabla \mathbf{u} = \boldsymbol{\varepsilon} + \boldsymbol{\omega}$  where  $\boldsymbol{\varepsilon} := \frac{1}{2} [\nabla \mathbf{u} + \nabla(\mathbf{u})^T]$  is the infinitesimal strain tensor with  $\nabla \times \boldsymbol{\varepsilon} = e_{ijk} \varepsilon_{rj,i} \mathbf{e}_k \otimes \mathbf{e}_r$ , and  $\boldsymbol{\omega} := \frac{1}{2} [\nabla \mathbf{u} - \nabla(\mathbf{u})^T]$  is the infinitesimal rotation tensor.

#### 3.1 Compatibility condition:

In the context of infinitesimal strain theory, we seek to find  $\mathbf{u} : \Omega \rightarrow \mathbb{R}^{n_{dim}}$  and corresponding  $\boldsymbol{\varepsilon} : \Omega \rightarrow \mathbb{R}^{n_{dim} \times n_{dim}}$ , and  $\boldsymbol{\sigma} : \Omega \rightarrow \mathbb{R}^{n_{dim} \times n_{dim}}$  for a given infinite elastic solid satisfying the following compatibility conditions (Marsden and Hughes, 1994):

$$\mathbf{R} := \nabla \times (\nabla \times \boldsymbol{\varepsilon})^T = \mathbf{0}; \quad (10)$$

where,  $\mathbf{R}$  is Saint-Venant compatibility tensor. Alternatively, the elastic solid should satisfy the Navier–Cauchy equations which can be expressed as (Lurie, 2010):

$$\begin{aligned} (\lambda + \mu)\nabla(\nabla \cdot \mathbf{u}) + \mu\Delta\mathbf{u} + \mathbf{B} &= \mathbf{0}, \quad \text{in } \Omega \\ \mathbf{u} |_{\Gamma_D} &= \bar{\mathbf{u}}, \end{aligned} \tag{11}$$

where  $\mathbf{u} = (u_1, u_2, \dots, u_{n_{dim}})$  is the unknown displacement field;  $\mu > 0$  and  $\lambda > -\mu$  are Lamé constants;  $\nabla$ ,  $\Delta$ , and  $\nabla$  represent the gradient, the Laplacian, and the divergence operators, respectively. Equation 11 satisfies the continuity of the displacement field  $\mathbf{u}$  and Dirichlet boundary condition.

### 3.2 Equilibrium condition:

In addition, the equilibrium condition and the Neumann boundary condition should be satisfied which can be expressed as (Marsden and Hughes, 1994):

$$\begin{aligned} \nabla \cdot \boldsymbol{\sigma} + \mathbf{B} &= \mathbf{0}, \quad \text{in } \Omega \\ \mathbf{t} := \mathbb{T}\mathbf{u} &= \bar{\mathbf{t}}, \quad \text{on } \Gamma_t \quad \boldsymbol{\sigma} |_{\Gamma_t} \hat{\mathbf{n}} = \bar{\mathbf{t}} \end{aligned} \tag{12}$$

where,  $\bar{\mathbf{t}}$  is a prescribed function on  $\Gamma_t$ ;  $\hat{\mathbf{n}}$  is the field normal to  $\Gamma_t$ . Equation 12 satisfies the momentum equation and the Neumann boundary condition where  $\mathbb{T}$  follows the conformal derivative operator such that (Atkin and Fox, 2005)

$$\mathbb{T}\mathbf{u} = \lambda(\Delta\mathbf{u}) \cdot \hat{\mathbf{n}} + 2\mu\frac{\partial\mathbf{u}}{\partial\hat{\mathbf{n}}} + \mu\hat{\mathbf{n}} \times (\nabla \times \mathbf{u}) \tag{13}$$

### 3.3 Constitutive relation:

Subsequently, the elastic constitutive relation can be expressed from generalized Hooke's law (Timoshenko, 1970) as:

$$\boldsymbol{\sigma} = \mathbf{C} : \boldsymbol{\varepsilon} \tag{14}$$

where, the fourth-order stiffness tensor  $\mathbf{C} = C_{ijkl}\mathbf{e}_i \otimes \mathbf{e}_j \otimes \mathbf{e}_k \otimes \mathbf{e}_l$  denotes the constitutive relation that maps the displacement gradient  $\nabla\mathbf{u}$  to the Cauchy stress tensor  $\boldsymbol{\sigma}$ . For an isotropic linearly elastic material,  $C_{ijkl} = \lambda\delta_{ij}\delta_{kl} + \mu(\delta_{ik}\delta_{jl} + \delta_{il}\delta_{jk})$  where  $\delta_{ij}$  is the Kronecker

delta. The components of the stress tensor  $\boldsymbol{\sigma}$ , and the strain tensor  $\boldsymbol{\varepsilon}$ , are expressed as :

$$\sigma_{ij}(\mathbf{u}) = \lambda \delta_{ij} \sum_{k=1}^{n_{dim}} \varepsilon_{kk}(\mathbf{u}) + 2\mu \varepsilon_{ij}(\mathbf{u}), \quad \varepsilon_{ij}(\mathbf{u}) = \frac{1}{2} \left( \frac{\partial u_i}{\partial x_j} + \frac{\partial u_j}{\partial x_i} \right), \quad i, j = 1, 2, \dots, n_{dim}. \quad (15)$$

Note that  $\boldsymbol{\sigma}$  is the Cauchy stress tensor in linear elasticity applicable under small deformation.

The constitutive relation in terms of strain can be alternatively expressed as,

$$\varepsilon_{ij,kl} + \varepsilon_{kl,ij} - \varepsilon_{ik,jl} - \varepsilon_{jl,ik} = 0 \quad i, j, k, l \in 1, 2, \dots, n_{dim}. \quad (16)$$

Equations governing a linear elastic boundary value problem (BVP) are defined by Eqs. 11–16 where the field variables  $\mathbf{u}, \boldsymbol{\sigma}, \boldsymbol{\varepsilon}$  can be obtained for given material constants (Atkin and Fox, 2005; Lurie, 2010).

#### 4. PINNs formulation for continuum linear elasticity:

The proposed PINNs framework is applied to linearly elastic solids. A two-dimensional ( $n_{dim} = 2$ ) problem is considered. The input features (variables) to the models are the spatial coordinates  $\mathbf{x} = (x, y)$ . A separate NN is used to approximate each output field variable. As shown in Fig. 1, displacement  $\mathbf{u}(\mathbf{x})$ , stress  $\boldsymbol{\sigma}(\mathbf{x})$ , and strain  $\boldsymbol{\varepsilon}(\mathbf{x})$  fields are obtained by densely connected independent ANNs. For  $n_{dim} = 2$ , considering symmetry of the stress and strain tensors,  $\mathbf{u}(\mathbf{x})$ ,  $\boldsymbol{\sigma}(\mathbf{x})$ , and  $\boldsymbol{\varepsilon}(\mathbf{x})$  fields can be approximated as:

$$\mathbf{u}(\mathbf{x}) \simeq \Xi_{\mathbf{u}}^{\text{NN}}(\mathbf{x}) = \begin{bmatrix} \tilde{\mathbf{u}}_x^{\text{NN}}(\mathbf{x}) \\ \tilde{\mathbf{u}}_y^{\text{NN}}(\mathbf{x}) \end{bmatrix} \quad (17)$$

$$\boldsymbol{\sigma}(\mathbf{x}) \simeq \Xi_{\boldsymbol{\sigma}}^{\text{NN}}(\mathbf{x}) = \begin{bmatrix} \tilde{\sigma}_{xx}^{\text{NN}}(\mathbf{x}) & \tilde{\sigma}_{xy}^{\text{NN}}(\mathbf{x}) \\ \tilde{\sigma}_{yx}^{\text{NN}}(\mathbf{x}) & \tilde{\sigma}_{xy}^{\text{NN}}(\mathbf{x}) \end{bmatrix}; \quad \boldsymbol{\varepsilon}(\mathbf{x}) \simeq \Xi_{\boldsymbol{\varepsilon}}^{\text{NN}}(\mathbf{x}) = \begin{bmatrix} \tilde{\varepsilon}_{xx}^{\text{NN}}(\mathbf{x}) & \tilde{\varepsilon}_{xy}^{\text{NN}}(\mathbf{x}) \\ \tilde{\varepsilon}_{yx}^{\text{NN}}(\mathbf{x}) & \tilde{\varepsilon}_{xy}^{\text{NN}}(\mathbf{x}) \end{bmatrix} \quad (18)$$

Here  $\Xi_{\mathbf{u}}^{\text{NN}}(\mathbf{x})$ ,  $\Xi_{\boldsymbol{\sigma}}^{\text{NN}}(\mathbf{x})$ , and  $\Xi_{\boldsymbol{\varepsilon}}^{\text{NN}}(\mathbf{x})$  denote the NN approximations for  $\mathbf{u}(\mathbf{x})$ ,  $\boldsymbol{\sigma}(\mathbf{x})$ , and  $\boldsymbol{\varepsilon}(\mathbf{x})$ , respectively.

##### 4.1 Loss function:

To define the loss function for the linear elasticity problem, governing equations including compatibility conditions, equilibrium conditions, constitutive relations, and boundary conditions that fully describe the problem have been considered. Additionally, as in a data-driven

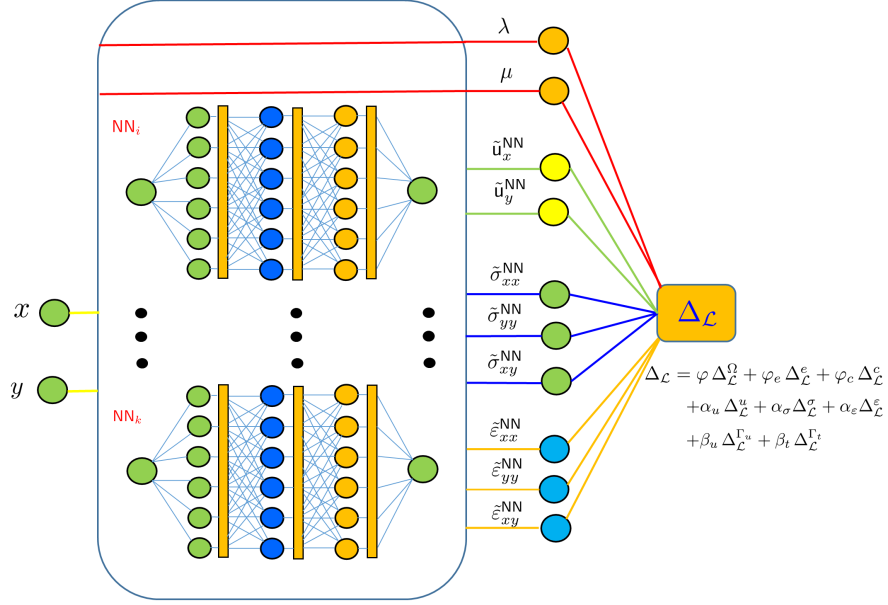


Figure 1: PINNs network architecture for solving linear elasticity problem consisting of multi-ANN ( $\text{NN}_i \forall i = 1, k$ ) for each output variables  $\tilde{u}_x^{\text{NN}}(\mathbf{x})$ ,  $\tilde{u}_y^{\text{NN}}(\mathbf{x})$ ,  $\tilde{\sigma}_{xx}^{\text{NN}}(\mathbf{x})$ ,  $\tilde{\sigma}_{yy}^{\text{NN}}(\mathbf{x})$ ,  $\tilde{\sigma}_{xy}^{\text{NN}}(\mathbf{x})$ ,  $\tilde{\epsilon}_{xx}^{\text{NN}}(\mathbf{x})$ , and  $\tilde{\epsilon}_{xy}^{\text{NN}}(\mathbf{x})$ , with independent variable  $\mathbf{x} = (x, y)$  as input features.

approach, the field variables in Eq. 8 have been included. The generalized multi-objective loss functional  $\Delta_{\mathcal{L}}$  can be expressed as:

$$\Delta_{\mathcal{L}}(\mathbf{x}, \theta) = \varphi \Delta_{\mathcal{L}}^{\Omega} + \varphi_e \Delta_{\mathcal{L}}^e + \varphi_c \Delta_{\mathcal{L}}^c + \beta_u \Delta_{\mathcal{L}}^{\Gamma_u} + \beta_t \Delta_{\mathcal{L}}^{\Gamma_t} + \alpha_{\mathbf{u}} \Delta_{\mathcal{L}}^{\mathbf{u}} + \alpha_{\boldsymbol{\sigma}} \Delta_{\mathcal{L}}^{\boldsymbol{\sigma}} + \alpha_{\boldsymbol{\epsilon}} \Delta_{\mathcal{L}}^{\boldsymbol{\epsilon}} \quad (19)$$

where,  $\Delta_{\mathcal{L}}^e$ ,  $\Delta_{\mathcal{L}}^c$ , and  $\Delta_{\mathcal{L}}^{\Omega}$  are the loss components from the equilibrium condition (Eq. 12), constitutive relation (Eq. 14), and the compatibility condition (Eq. 15), respectively;  $\Delta_{\mathcal{L}}^{\Gamma_u}$  and  $\Delta_{\mathcal{L}}^{\Gamma_t}$  represent the loss components computed at the Dirichlet boundary  $\Gamma_u$ , and the Neumann boundary  $\Gamma_t$  (Eq. 11), respectively;  $\Delta_{\mathcal{L}}^{\mathbf{u}}$ ,  $\Delta_{\mathcal{L}}^{\boldsymbol{\sigma}}$ , and  $\Delta_{\mathcal{L}}^{\boldsymbol{\epsilon}}$  are the loss components for the fields  $\mathbf{u}(\mathbf{x})$ ,  $\boldsymbol{\sigma}(\mathbf{x})$ , and  $\boldsymbol{\epsilon}(\mathbf{x})$ , respectively, when a data driven approach is pursued. The coefficients  $\varphi, \varphi_e, \varphi_c, \beta_u, \beta_t, \alpha_{\mathbf{u}}, \alpha_{\boldsymbol{\sigma}}$ , and  $\alpha_{\boldsymbol{\epsilon}}$  are the weights associated with each loss term that dictates the emphasis on each penalty term. Evidently, the terms in the cost function are the measures of the errors in the displacement and stress fields, the momentum balance, and the constitutive

law. The explicit expression for each term in  $\Delta_{\mathcal{L}}(\mathbf{x}, \theta)$  is,

$$\Delta_{\mathcal{L}}^{\Omega} = \frac{1}{N_c^{\Omega}} \sum_{l=1}^{N_c^{\Omega}} \|\nabla \cdot \Xi_{\boldsymbol{\sigma}}^{\text{NN}}(\mathbf{x}_{l|\Omega}) + \mathbf{B}(\mathbf{x}_{l|\Omega})\| \quad (20)$$

$$\Delta_{\mathcal{L}}^c = \frac{1}{N_c^{\Omega}} \sum_{l=1}^{N_c^{\Omega}} \|\Xi_{\boldsymbol{\sigma}}^{\text{NN}}(\mathbf{x}_{l|\Omega}) - \mathbf{C} [\nabla \cdot \Xi_{\mathbf{u}}^{\text{NN}}(\mathbf{x}_{l|\Omega})]\| \quad (21)$$

$$\Delta_{\mathcal{L}}^{\Gamma_u} = \frac{1}{N_c^{\Gamma_u}} \sum_{k=1}^{N_c^{\Gamma_u}} \|\Xi_{\mathbf{u}}^{\text{NN}}(\mathbf{x}_{k|\Gamma_u}) - \bar{\mathbf{u}}(\mathbf{x}_{k|\Gamma_u})\| \quad (22)$$

$$\Delta_{\mathcal{L}}^{\Gamma_t} = \frac{1}{N_c^{\Gamma_t}} \sum_{j=1}^{N_c^{\Gamma_t}} \|\Xi_{\boldsymbol{\sigma}}^{\text{NN}}(\mathbf{x}_{j|\Gamma_t}) \hat{\mathbf{n}} - \bar{\mathbf{t}}(\mathbf{x}_{j|\Gamma_t})\| \quad (23)$$

$$\Delta_{\mathcal{L}}^{\mathbf{u}} = \frac{1}{N_c^{\Omega}} \sum_{l=1}^{N_c^{\Omega}} \|\Xi_{\mathbf{u}}^{\text{NN}}(\mathbf{x}_{l|\Omega}) - \hat{\mathbf{u}}(\mathbf{x}_{l|\Omega})\| \quad (24)$$

$$\Delta_{\mathcal{L}}^{\boldsymbol{\sigma}} = \frac{1}{N_c^{\Omega}} \sum_{l=1}^{N_c^{\Omega}} \|\Xi_{\boldsymbol{\sigma}}^{\text{NN}}(\mathbf{x}_{l|\Omega}) - \hat{\boldsymbol{\sigma}}(\mathbf{x}_{l|\Omega})\| \quad (25)$$

$$\Delta_{\mathcal{L}}^{\boldsymbol{\varepsilon}} = \frac{1}{N_c^{\Omega}} \sum_{l=1}^{N_c^{\Omega}} \|\Xi_{\boldsymbol{\varepsilon}}^{\text{NN}}(\mathbf{x}_{l|\Omega}) - \hat{\boldsymbol{\varepsilon}}(\mathbf{x}_{l|\Omega})\| \quad (26)$$

where,  $\{\mathbf{x}_{1|\Omega}, \dots, \mathbf{x}_{N_c^{\Omega}|\Omega}\}$  are randomly chosen collocation points over the domain  $\Omega$ ;  $\{\mathbf{x}_{1|\Gamma_u}, \dots, \mathbf{x}_{N_c^{\Gamma_u}|\Gamma_u}\}$  and  $\{\mathbf{x}_{1|\Gamma_t}, \dots, \mathbf{x}_{N_c^{\Gamma_t}|\Gamma_t}\}$  are those chosen randomly along the boundaries  $\Gamma_u$  and  $\Gamma_t$ , respectively. The terms  $\hat{\mathbf{u}}(\mathbf{x}_{l|\Omega})$ ,  $\hat{\boldsymbol{\sigma}}(\mathbf{x}_{l|\Omega})$ , and  $\hat{\boldsymbol{\varepsilon}}(\mathbf{x}_{l|\Omega})$  represent the true (target) value obtained by means of analytical solution or high-fidelity simulation. The weights  $\varphi, \varphi_e, \varphi_c \in \mathbb{R}^+$  are the weights corresponding to the compatibility, equilibrium, and constitutive relations, respectively. In general, these coefficients can be prescribed as 1 for solving a relatively less complex problem, whereas,  $\beta_u$  and  $\beta_t$  are the binary (i.e., either 0 or 1) integers. The weights  $\alpha_i = 1; \forall i = \mathbf{u}, \boldsymbol{\sigma}, \boldsymbol{\varepsilon}$  for a complete data driven approach for  $\mathbf{u}(\mathbf{x})$ ,  $\boldsymbol{\sigma}(\mathbf{x})$ , and  $\boldsymbol{\varepsilon}(\mathbf{x})$ , respectively at the collocation points  $N_c^{\Omega}$ . However, we prescribe  $\alpha_i = 0 \forall (i = \mathbf{u}, \boldsymbol{\sigma}, \boldsymbol{\varepsilon})$  as labeled training data is unavailable, which may not guarantee the accuracy of PINNs solutions.

The forward problem is studied herein, where the displacement, stress, and strain fields are obtained as the PINNs solutions assuming material properties  $\lambda$  and  $\mu$  remain constant. However, the loss functional in Eq. 19 can also be utilized in an inverse problem for parameter identification, where  $\lambda$  and  $\mu$  can be treated as network outputs which may vary during training (Fig. 1). For the network construction in the PINNs framework, SciANN (Haghighat and

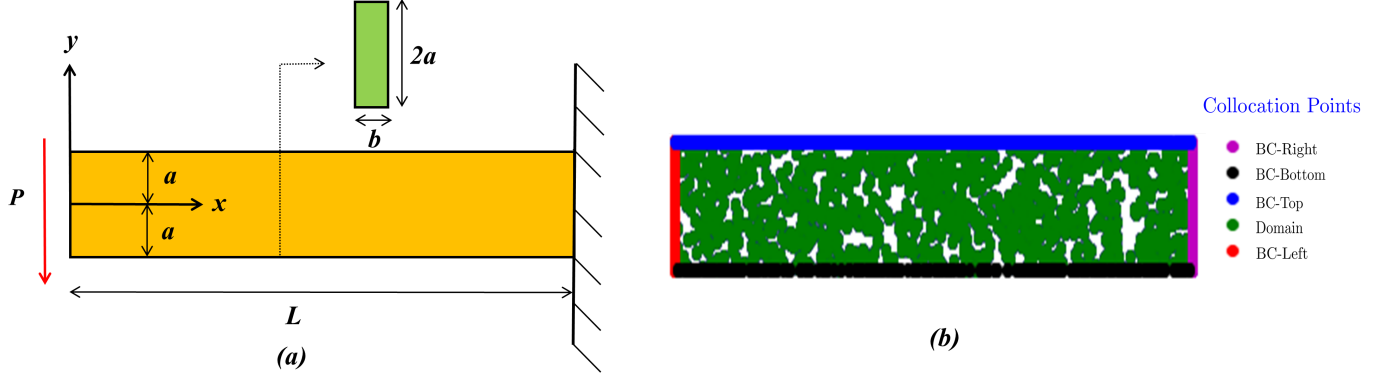


Figure 2: (a) Elastic plane-stress problem for an end-loaded cantilever beam of length  $L$ , height  $2a$  and out-of-plane thickness  $b$  which has been clamped at  $x = L$ ; (b) distributions of total collocation points  $N_c = 5,000$  on the problem domain and various boundaries during PINNs training.

(Juanes, 2021), a convenient high-level Keras (Chollet et al., 2015) wrapper for PINNs is used.

## 4.2 Solution for linear elasticity problem :

For this study, an end-loaded isotropic linearly elastic cantilever beam of height  $2a$ , length  $L$ , thickness  $b$  (assuming  $b \ll a$ ) has been considered to ensure a state of plane-stress condition as shown in Fig. 2. The left edge of the beam is subjected to a resultant force  $P$ . Whereas, the right-hand end is clamped. The top and bottom surfaces of the beam,  $y = \pm a$  are traction free. An approximate solution to the problem can be obtained from the Airy function discussed next.

### 4.2.1 The Airy solution to the end-loaded cantilever beam:

The Airy solution in Cartesian coordinates  $\Omega \subset \mathbb{R}^2$  can be found from the Airy potential  $\phi(x, y)$  that satisfies (Bower, 2009),

$$\nabla^4 \phi = \frac{\partial^4 \phi}{\partial x^4} + 2 \frac{\partial^4 \phi}{\partial x^2 \partial y^2} + \frac{\partial^4 \phi}{\partial y^4} = \mathbf{C}(\nu) \left( \frac{\partial b_x}{\partial x} + \frac{\partial b_y}{\partial y} \right) \quad (27)$$

where,

$$\mathbf{C}(\nu) = \begin{cases} \frac{1-\nu}{1-2\nu} & \text{(plane strain)} \\ \frac{1}{1-\nu} & \text{(plane stress)} \end{cases} \quad (28)$$

Here, the body forces  $b_x, b_y$  have the form  $\rho_0 b_x = \frac{\partial \Omega}{\partial x}$ ,  $\rho_0 b_y = \frac{\partial \Omega}{\partial y}$ ;  $\Omega(x, y)$  is the positional scalar function. The solution of the Airy function can be expressed in the polynomial form  $\phi(x, y) = \sum_{m=0}^{\infty} \sum_{n=0}^{\infty} A_{mn} x^m y^n$ . For  $m+n \leq 3$ , the terms automatically satisfy the biharmonic equation for any  $A_{mn}$ . Additionally,  $\phi$  must satisfy the following traction boundary conditions on  $\Omega$ .

$$\frac{\partial^2 \phi}{\partial y^2} n_x - \frac{\partial^2 \phi}{\partial x \partial y} n_y = t_x; \quad \frac{\partial^2 \phi}{\partial x^2} n_y - \frac{\partial^2 \phi}{\partial x \partial y} n_x = t_y \quad (29)$$

Here,  $(n_x, n_y)$  are the components of a unit vector normal to the boundary. For the end-loaded cantilever beam, the Airy function can be formulated as,

$$\phi = -\frac{3P}{4ab}xy + \frac{P}{4a^3b}xy^3 \quad (30)$$

where,  $\sigma_{xx} = \frac{\partial^2 \phi}{\partial y^2} - \Omega$ ;  $\sigma_{yy} = \frac{\partial^2 \phi}{\partial x^2} - \Omega$ ;  $\sigma_{xy} = \sigma_{yx} = -\frac{\partial^2 \phi}{\partial x \partial y}$  with  $\Omega = 0$ . At the clamped end,  $x_1 = L$ , displacement boundary conditions are  $u_x = u_y = \partial u_y / \partial x = 0$ . The top and bottom surfaces of the beam (i.e.,  $y = \pm a$ ) are traction free,  $\sigma_{ij} n_j = 0$ , that requires  $\sigma_{yy} = \sigma_{xy} = 0$ . Whereas, the resultant of the traction acting on the surface at  $x = 0$  is  $-Pe_y$  with traction vector  $t_i = \sigma_{ij} n_j = -\sigma_{xy} \delta_{iy} = -\frac{3P}{4ab}(1 - \frac{y^2}{a^2})\delta_{iy}$ . The resultant force can be obtained as :  $F_i = b \int_{-a}^a -\frac{3P}{4ab}(1 - \frac{y^2}{a^2})\delta_{iy} dx_2 = -P\delta_{iy}$ . On satisfaction of the aforementioned conditions, approximate analytical solutions for the displacements  $u_x, u_y$ , the strain fields  $\varepsilon_{xx}, \varepsilon_{yy}, \varepsilon_{xy}$  and the stress fields  $\sigma_{xx}, \sigma_{yy}, \sigma_{xy}$  can be expressed as:

$$u_x = \frac{3P}{4Ea^3b}x^2y - (2 + \mu)\frac{P}{4Ea^3b}y^3 + 3(1 + \mu)\frac{Pa^2}{2Ea^3b}y - \frac{3PL^2}{4Ea^3b}y \quad (31)$$

$$u_y = -\frac{3\mu P}{4Ea^3b}xy^2 - \frac{P}{4Ea^3b}x^3 + \frac{3PL^2}{4Ea^3b}x - \frac{PL^3}{2Ea^3b} \quad (32)$$

$$\varepsilon_{xx} = \frac{3P}{2Ea^3b}xy; \quad \varepsilon_{yy} = -\frac{3P\mu}{2Ea^3b}xy; \quad \varepsilon_{xy} = \frac{3P(1 + \mu)}{4Eab} \left(1 - \frac{y^2}{a^2}\right) \quad (33)$$

$$\sigma_{xx} = \frac{3P}{2a^3b}xy; \quad \sigma_{yy} = 0; \quad \sigma_{xy} = \frac{3P}{4ab} \left(1 - \frac{y^2}{a^2}\right) \quad (34)$$

These analytical solutions for  $\mathbf{u}(\mathbf{x})$ ,  $\boldsymbol{\sigma}(\mathbf{x})$ , and  $\boldsymbol{\varepsilon}(\mathbf{x})$  have been used as  $\hat{\mathbf{u}}(\mathbf{x}|_{\Omega})$ ,  $\hat{\boldsymbol{\sigma}}(\mathbf{x}|_{\Omega})$ , and  $\hat{\boldsymbol{\varepsilon}}(\mathbf{x}|_{\Omega})$  at the collocation points for data-driven enhancement in Eqs. 24-26, respectively, for solving the field variables in the proposed PINNs framework.

#### 4.2.2 PINNs solutions for linear elasticity problem:

For the benchmark, end-loaded cantilever beam problem,  $L = 3$  m,  $a = 0.5$  m, and  $b = 0.001$



m have been considered. The material properties are, Young's modulus  $E = 1$  GPa, and the Poisson ratio  $\nu = 0.25$  as shown in Fig. 2 -(a). Unless otherwise stated, a total of  $N_c = 5,000$  randomly distributed collocation points over the domain and boundaries have been used for training the PINNs model as shown in Fig. 2 -(a). During training, the optimization loop was run for 500 epochs using the Adam optimization scheme with a learning rate of 0.001, and a batch size of 32 for optimal accuracy and faster convergence.

The Airy solutions for various fields including displacements  $u_x$ ,  $u_y$ , stresses  $\sigma_{xx}$ ,  $\sigma_{yy}$ ,  $\sigma_{xy}$ , and strains  $\varepsilon_{xx}$ ,  $\varepsilon_{yy}$ ,  $\varepsilon_{xy}$  as in Eqs. 31-34 are shown in Fig. 3-(a). The corresponding PINNs approximations using the tanh activation function are shown in Fig. 3 -(b). Additionally, in Fig. 3 -(c), the absolute error between the Airy solutions and PINNs predictions for each field variable is shown. The overall results from PINNs are in excellent agreement with the Airy solutions. The PINNs approximations attained satisfactory accuracy with low absolute errors for all field variables. For the displacement fields, the absolute error is relatively high near to clamped edge for  $u_x$ . For  $u_y$ , the absolute error is maximum at the midsection and near the horizontal edges as shown in Fig. 3 -(c). This is due to the approximate nature of the Airy solutions at clamped end  $x_1 = L$  for the displacement boundary conditions  $u_x = u_y = \partial u_y / \partial x = 0$ . Such differences also propagate through the solutions of stress and strain fields, where PINNs predictions slightly deviate from the Airy solutions, in particular, near the free vertical and horizontal edges as shown in Fig. 3 -(c). However, according to Saint-Venant's principle, these deviations do not sufficiently influence the solution far from the end, which is reflected in the result. Overall, the proposed PINNs model can capture the distributions of various fields accurately from the solution of the Airy stress function.

### 4.2.3 Suitable activation function :

The impact of the use of various activation functions on training the PINNs models in predicting field variables and the epoch evolution of various components of the loss function is explored. The ReLU, sigmoid, and tanh activation functions are compared; the network architecture remains the same: the number of neurons in each layer  $\mathcal{N} = 20$  with the total number of hidden layers  $L_n = 5$  in the PINNs model. The evolution of the total loss  $\Delta_{\mathcal{L}}$ , and the

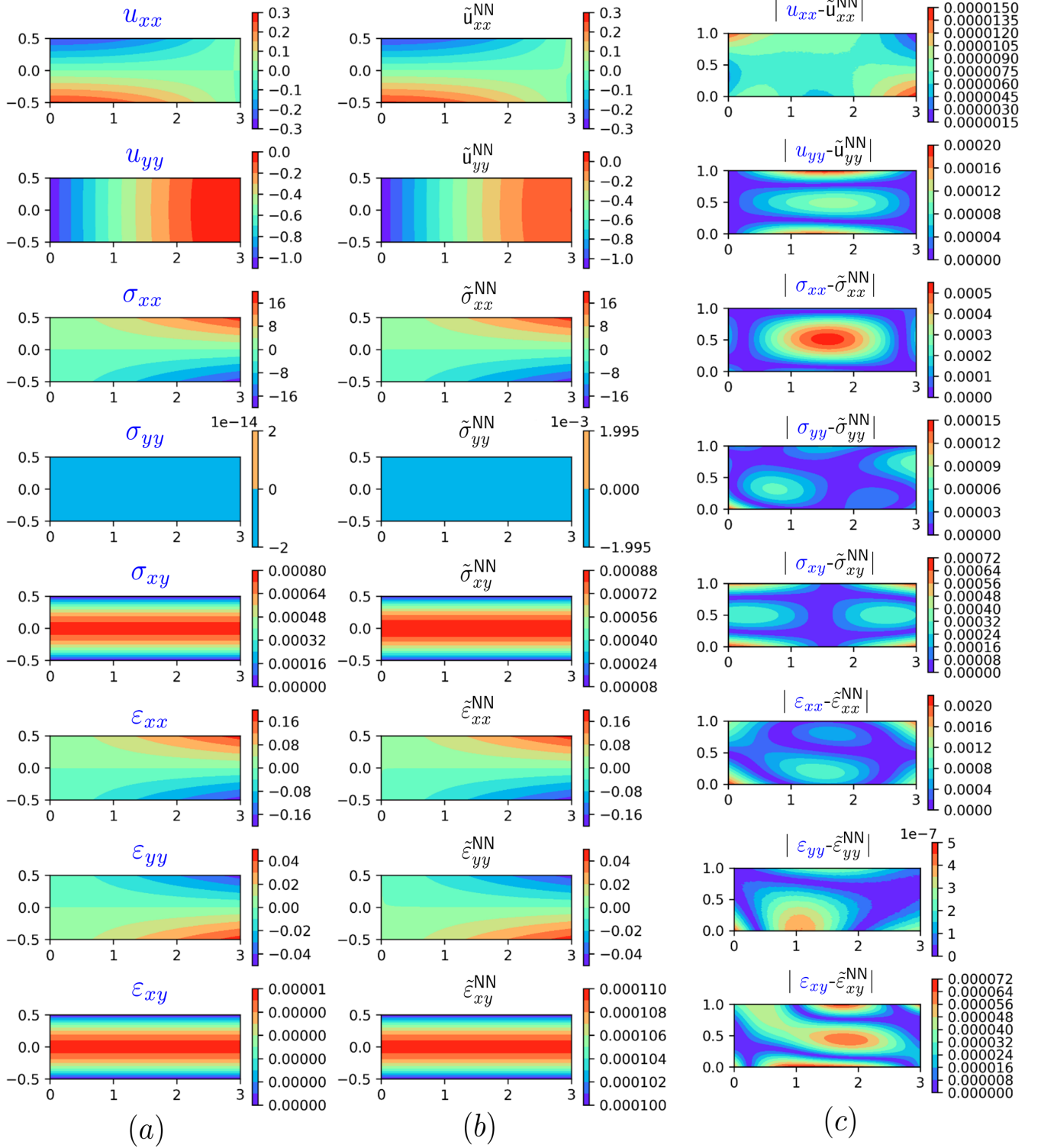


Figure 3: (a) The Airy solutions for displacements  $u_x$ ,  $u_y$ , stresses  $\sigma_{xx}$ ,  $\sigma_{yy}$ ,  $\sigma_{xy}$ , strains  $\varepsilon_{xx}$ ,  $\varepsilon_{yy}$ ,  $\varepsilon_{xy}$ ; (b) corresponding PINNs solutions for  $\tilde{u}_x^{NN}$ ,  $\tilde{u}_y^{NN}$ ,  $\tilde{\sigma}_{xx}^{NN}$ ,  $\tilde{\sigma}_{yy}^{NN}$ ,  $\tilde{\sigma}_{xy}^{NN}$ ,  $\tilde{\varepsilon}_{xx}^{NN}$ ,  $\tilde{\varepsilon}_{yy}^{NN}$ , and  $\tilde{\varepsilon}_{xy}^{NN}$ ; (c) absolute error between the Airy solutions and PINNs predictions associated with each field variables for an end-loaded cantilever beam.

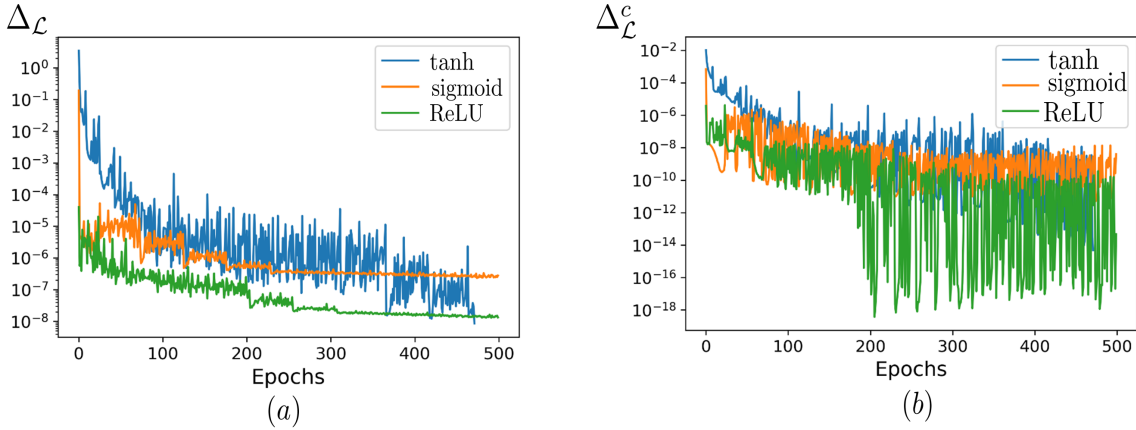


Figure 4: Comparison of (a) total loss  $\Delta_{\mathcal{L}}^{\Omega}$ ; (b) constitutive loss  $\Delta_{\mathcal{L}}^c$  for tanh, sigmoid and ReLU activation functions for network parameters  $\mathcal{N} = 20, L_n = 5$ .

constitutive loss  $\Delta_{\mathcal{L}}^c$  are depicted in Fig. 4. Additionally, values of the various loss components and training times  $t_{tr}$  at the end of training are compared in Table. 1. Evidently, the tanh activation provides the best performance in terms of the value of the total loss at the end of training. The final constitutive loss with tanh activation is significantly lower compared to the other two activations illustrating the suitability of the use of the tanh activation for the PINNs model for solving the elasticity problem herein. In addition, all other loss components obtained are lowest upon using the tanh activation as shown in Table 1.

Comparing the evolution of  $\Delta_{\mathcal{L}}$ , the convergence characteristics for the ReLU activation are better compared to the tanh with fewer fluctuations and rapid decrease in loss values as shown in Fig. 4-(a). However, the tanh illustrates better adaptability in the constitutive loss with an excellent convergence rate in Fig. 4-(b). Out of the three activations, ReLU performs the worst possibly due to its derivative being discontinuous. However, the total loss for all three activations is negligible (loss value in the range below  $10^{-4}$  to  $10^{-5}$ ) within 200 epochs indicating the adaptability of the proposed PINNs framework to any of these activations provided the models are trained sufficiently long. In comparing the training time, the tanh activation takes longer for the same number of epochs compared to the other two. This coincides with the fact that the evolution of the total loss has a higher degree of discontinuity. However, the model with the ReLU activation trains the fastest possibly due to its linear nature. From the comparison, it can be concluded that although tanh is the best in terms of accuracy, however, ReLU can be an optimal choice of activation considering both accuracy and training time for

Table 1: Influence of different activation functions on the final values of various loss components (in  $10^{-09}$ ) and training times  $t_{tr}$  in the proposed PINNs model for solving linear elastic beam problem.

| Activation Function | $\Delta_{\mathcal{L}}^{\Omega}$ | $\Delta_{\mathcal{L}}^c$ | $\Delta_{\mathcal{L}}^{\Gamma_u}$ | $\Delta_{\mathcal{L}}^{\Gamma_t}$ | $\Delta_{\mathcal{L}}^{\mathbf{u}}$ | $\Delta_{\mathcal{L}}^{\boldsymbol{\sigma}}$ | $\Delta_{\mathcal{L}}^{\boldsymbol{\varepsilon}}$ | $\Delta_{\mathcal{L}}$ | $t_{tr}$<br>(min) |
|---------------------|---------------------------------|--------------------------|-----------------------------------|-----------------------------------|-------------------------------------|--|---|------------------------|-------------------|
| ReLU                | 107.16                          | 43.43                    | 14.51                             | 36.75                             | 24.97                               | 1.07   | 5.48  | 233.37                 | 9.4               |
| Sigmoid             | 30.96                           | 54.33                    | 517.38                            | 126.14                            | 37.85                               | 124.51                                       | 592.82  | 1483.99                | 13.8              |
| tanh                | 4.56                            | 0.73                     | 31.47                             | 25.64                             | 3.11                                | 9.60   | 10.45   | 85.56                  | 15.7              |

Table 2: Influence of network parameters  $\mathcal{N}$  and  $L_n$  on training times  $t_{tr}$  and final values various loss components (in  $10^{-09}$ ) for tanh activation.

| Network identifier                   | $n_p$   | $t_{tr}$<br>(min) | $\Delta_{\mathcal{L}}^{\Omega}$ | $\Delta_{\mathcal{L}}^c$ | $\Delta_{\mathcal{L}}^{\Gamma_u}$ | $\Delta_{\mathcal{L}}^{\Gamma_t}$ | $\Delta_{\mathcal{L}}^{\mathbf{u}}$ | $\Delta_{\mathcal{L}}^{\boldsymbol{\sigma}}$ | $\Delta_{\mathcal{L}}^{\boldsymbol{\varepsilon}}$ | $\Delta_{\mathcal{L}}$ |
|--------------------------------------|---------|-------------------|---------------------------------|--------------------------|-----------------------------------|-----------------------------------|-------------------------------------|--|---|------------------------|
| N-1 ( $\mathcal{N} = 20, L_n = 5$ )  | 22,706  | 15.7              | 4.56                            | 0.73                     | 31.47                             | 25.64                             | 3.11                                | 9.60   | 10.45   | 85.56                  |
| N-2 ( $\mathcal{N} = 40, L_n = 5$ )  | 113,530 | 23.8              | 2.21                            | 90.39                    | 77.73                             | 59.58                             | 4.29                                | 24.16  | 78.39   | 336.75                 |
| N-3 ( $\mathcal{N} = 20, L_n = 10$ ) | 54,494  | 18.3              | 6.89                            | 0.89                     | 12.73                             | 65.42                             | 13.01                               | 17.19  | 4.67  | 120.8                  |
| N-4 ( $\mathcal{N} = 40, L_n = 10$ ) | 272,472 | 32.3              | 2.78                            | 3.67                     | 18.78                             | 12.63                             | 24.19                               | 43.10  | 2.49  | 107.64                 |

solving elasticity equation in the proposed PINNs framework.

#### 4.2.4 Influence of network complexity:

It is worth mentioning that the PINNs approximations are sensitive to network architecture including the depth of the hidden layer and the number of network parameters. In this section, the influence of network architecture parameters, i.e., the number of neurons in each hidden layer  $\mathcal{N}$ , and the number of hidden layers  $L_n$  on the accuracy and the efficiency of the PINNs solution are explored. Since the tanh activation performs the best in terms of accuracy (see previous section), it is chosen as the activation for different networks used in the following experiments.

In the current study, four different networks considering the combinations  $\mathcal{N} = 20, 40$ , and  $L_n = 5, 10$  are tested, and values of different loss components at the end of the training, train-

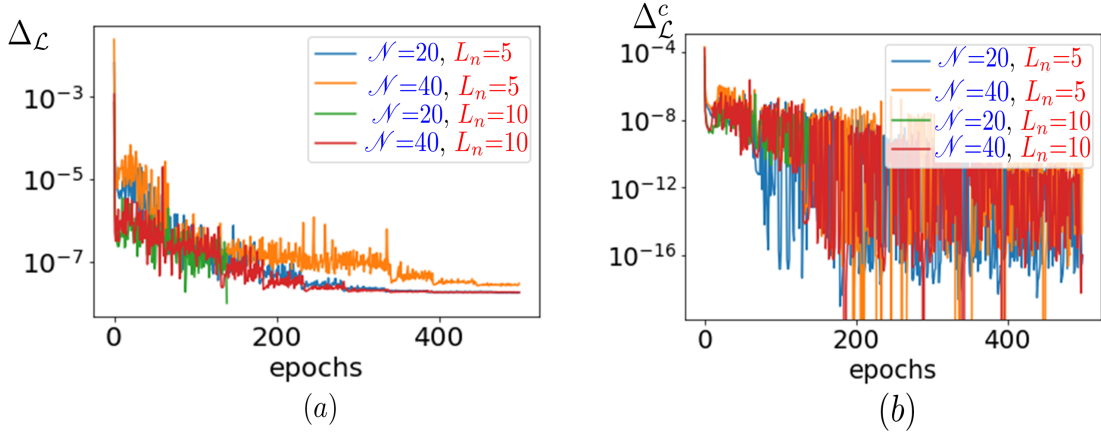


Figure 5: Comparison of (a) total loss  $\Delta_{\mathcal{L}}^{\Omega}$ ; (b) constitutive loss  $\Delta_{\mathcal{L}}^c$  for various combinations of network parameters  $\mathcal{N}$  and  $L_n$  considering tanh activation function.

ing duration ( $t_{tr}$ ), along with model complexities in terms of network parameters ( $n_p$ ) for these architectures are presented in Table. 2. For fair comparison,  $N_c = 5,000$  for all experiments. The evolution of the total loss  $\Delta_{\mathcal{L}}$  and the constitutive loss  $\Delta_{\mathcal{L}}^{\Omega}$  for these networks are shown in Fig. 5. From the comparisons, for the chosen number of collocation points relatively shallow network  $\mathcal{N} = 20$ ,  $L_n = 5$  provides the best performance in terms of  $\Delta_{\mathcal{L}}$  and  $\Delta_{\mathcal{L}}^{\Omega}$  at the end of training. Additionally, the time required for training is faster due to a significantly lower number of network parameters. However, for a relatively deeper network,  $\mathcal{N} = 20$ ,  $L_n = 10$  with increased network complexity, the performance of the model degrades with respect to loss values as shown in Table. 2 possibly due to an increase in variability and reduction in bias. Interestingly, an increase in the number of neurons  $\mathcal{N} = 40$  while maintaining the depth of the network ( $L_n = 5$ ) leads to the worst performance which can be attributed to over-fitting (Bilbao and Bilbao, 2017; Jabbar and Khan, 2015). The epoch evolution of the loss for various network architectures demonstrates the efficacy of a relatively shallow network with significantly faster training for solving elasticity problems in the proposed PINNs framework.

## 5. PINNs formulation for linear elastic plate theory :

In this section, the PINNs framework is expanded for the solution of the classical Kirchhoff-Love thin plate (Timoshenko and Woinowsky-Krieger, 1959) subjected to a transverse loading in linearly elastic plate theory. In the subsequent section, the Kirchhoff-Love theory has been

briefly described; PINNs formulation for solving the governing fourth-order biharmonic partial differential equation (PDE) for the solution of the thin plate is elaborated. For a benchmark problem, the proposed PINNs approach is applied for the solution of a simply supported rectangular plate under a transverse sinusoidal loading condition.

### 5.1 Kirchhoff-Love thin plate theory :

Thin plates are structurally planar elements that have small thickness relative to their in-plane dimensions which can be simplified as a two-dimensional plate problem. According to the Kirchhoff-Love theory, the kinetics of a thin plate under the effect of a distributed transverse loading  $q = q(x, y)$  can be described by a fourth-order differential equation (Timoshenko and Woinowsky-Krieger, 1959; Reddy, 2006).

$$\Delta(\mathcal{D}\Delta w) = q \quad (35)$$

When the elastic plate is bounded in the domain  $\Omega \subset \mathbb{R}^2$ , Eq. 35 is known as the Kirchhoff-Love equation. In Cartesian coordinates,  $w = w(x, y)$  represents the transverse displacement field,  $\mathcal{D} = \mathcal{D}(x, y)$  is the bending stiffness of the plate, and  $\Delta = \partial^2/\partial x^2 + \partial^2/\partial y^2$  is the Laplace operator. Considering a homogeneous and isotropic plate (i.e.,  $\mathcal{D} \equiv \text{constant}$ ), Eq. 35 becomes the biharmonic equation (Timoshenko and Woinowsky-Krieger, 1959; Szilard and Nash, 1974)

$$\mathcal{D}\Delta^2 w = \mathcal{D} \left( \frac{\partial^4 w}{\partial x^4} + 2\frac{\partial^4 w}{\partial x^2 \partial y^2} + \frac{\partial^4 w}{\partial y^4} \right) = q \quad (36)$$

Under appropriate boundary conditions, and with  $\mathcal{D}(x, y) > 0$  and  $q(x, y) \geq 0$ , both being known, the problem possesses a unique solution for the displacement  $w(x, y)$ . The set of solution variables includes the primitive variable deflection  $w$ , and the derived quantities, moments  $M_{xx}$ ,  $M_{yy}$ ,  $M_{xy} = -M_{yx}$ , and shearing forces  $Q_{xx}$ ,  $Q_{yy}$ . The expressions for the derived fields are,

$$M_{xx} = -\mathcal{D} \left( \frac{\partial^2 w}{\partial x^2} + \nu \frac{\partial^2 w}{\partial y^2} \right); \quad M_{yy} = -\mathcal{D} \left( \frac{\partial^2 w}{\partial y^2} + \nu \frac{\partial^2 w}{\partial x^2} \right); \quad M_{xy} = -\mathcal{D}(1 - \nu) \left( \frac{\partial^2 w}{\partial x \partial y} \right) \quad (37)$$

$$Q_{xx} = \frac{\partial M_{yx}}{\partial y} + \frac{\partial M_{xx}}{\partial x} = -\mathcal{D} \frac{\partial}{\partial x} \left( \frac{\partial^2 w}{\partial x^2} + \frac{\partial^2 w}{\partial y^2} \right); \quad Q_{yy} = \frac{\partial M_{yy}}{\partial y} - \frac{\partial M_{xy}}{\partial x} = -\mathcal{D} \frac{\partial}{\partial y} \left( \frac{\partial^2 w}{\partial x^2} + \frac{\partial^2 w}{\partial y^2} \right) \quad (38)$$

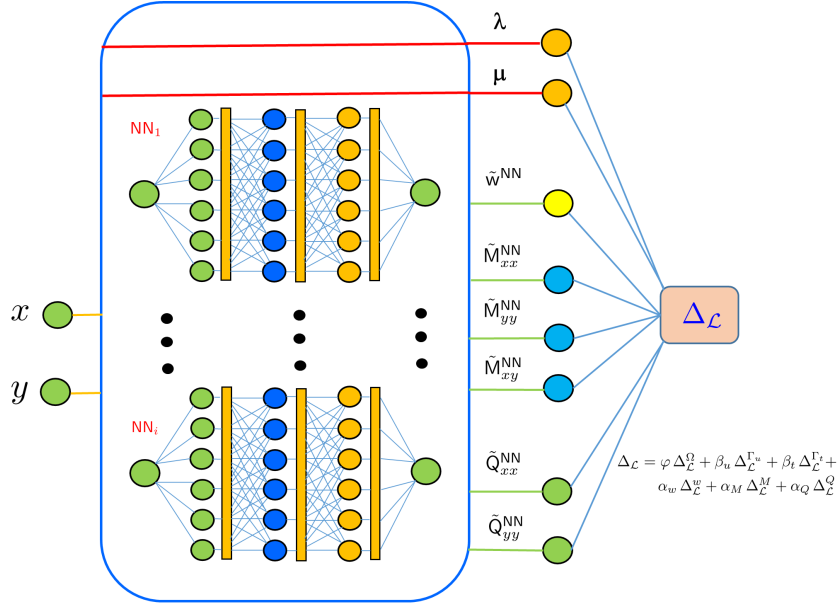


Figure 6: PINNs network architecture for solving Kirchhoff-Love thin plate problem governed by biharmonic equation consisting of multi-ANN ( $\text{NN}_i \forall i = 1, k$ ) for each field variables  $\tilde{w}^{\text{NN}}(\mathbf{x})$ ,  $\tilde{M}_{xx}^{\text{NN}}(\mathbf{x})$ ,  $\tilde{M}_{xy}^{\text{NN}}(\mathbf{x})$ ,  $\tilde{M}_{yy}^{\text{NN}}(\mathbf{x})$ ,  $\tilde{Q}_{xx}^{\text{NN}}(\mathbf{x})$ , and  $\tilde{Q}_{yy}^{\text{NN}}(\mathbf{x})$  with independent variable  $\mathbf{x} = (x, y)$  as input features.

## 5.2 PINNs formulation for the Biharmonic equation:

For solving the Biharmonic equation using the PINNs framework, the input features are the spatial coordinates  $\mathbf{x} := (x, y)$ ; the field variables,  $w(\mathbf{x})$ ,  $\mathbf{M}(\mathbf{x})$ , and  $\mathbf{Q}(\mathbf{x})$  are obtained using multiple densely connected independent ANNs, with each network approximating one of the outputs (Fig. 7). Different field variables approximated by the NNs are as follows:

$$w(\mathbf{x}) \simeq \Xi_w^{\text{NN}} = \tilde{w}^{\text{NN}}(\mathbf{x}) \quad (39)$$

$$\mathbf{M}(\mathbf{x}) \simeq \Xi_M^{\text{NN}} = \begin{bmatrix} \tilde{M}_{xx}^{\text{NN}}(\mathbf{x}) & \tilde{M}_{xy}^{\text{NN}}(\mathbf{x}) \\ \tilde{M}_{yx}^{\text{NN}}(\mathbf{x}) & \tilde{M}_{yy}^{\text{NN}}(\mathbf{x}) \end{bmatrix}; \quad \mathbf{Q}(\mathbf{x}) \simeq \Xi_Q^{\text{NN}} = \begin{bmatrix} \tilde{Q}_{xx}^{\text{NN}}(\mathbf{x}) \\ \tilde{Q}_{yy}^{\text{NN}}(\mathbf{x}) \end{bmatrix} \quad (40)$$

where,  $\Xi_w^{\text{NN}}$ ,  $\Xi_M^{\text{NN}}$ , and  $\Xi_Q^{\text{NN}}$  are the neural network approximations. From the NN approximations of the fields, the multi-objective loss function  $\Delta_{\mathcal{L}}(\mathbf{x}, \theta)$  can be defined as:

$$\Delta_{\mathcal{L}}(\mathbf{x}, \theta) = \varphi \Delta_{\mathcal{L}}^{\Omega} + \beta_u \Delta_{\mathcal{L}}^{\Gamma_u} + \beta_t \Delta_{\mathcal{L}}^{\Gamma_t} + \alpha_w \Delta_{\mathcal{L}}^w + \alpha_M \Delta_{\mathcal{L}}^M + \alpha_Q \Delta_{\mathcal{L}}^Q \quad (41)$$

where,  $\Delta_{\mathcal{L}}^{\Omega}$ ,  $\Delta_{\mathcal{L}}^{\Gamma_u}$ ,  $\Delta_{\mathcal{L}}^{\Gamma_t}$  are the losses in the domain  $\Omega$ , and along the boundaries  $\Gamma_u$  and  $\Gamma_t$ , respectively. Their expressions are,

$$\Delta_{\mathcal{L}}^{\Omega} = \frac{1}{N_c^{\Omega}} \sum_{l=1}^{N_c^{\Omega}} \left\| \nabla^2 \nabla^2 w - \frac{\hat{q}}{\mathcal{D}} \right\| \quad (42)$$

$$\Delta_{\mathcal{L}}^{\Gamma_u} = \frac{1}{N_c^{\Gamma_u}} \sum_{k=1}^{N_c^{\Gamma_u}} \left\| \Xi_{\mathbf{w}}^{\text{NN}}(\mathbf{x}_{k|\Gamma_u}) - \bar{w}(\mathbf{x}_{k|\Gamma_u}) \right\| \quad (43)$$

$$\Delta_{\mathcal{L}}^{\Gamma_t} = \frac{1}{N_c^{\Gamma_t}} \sum_{j=1}^{N_c^{\Gamma_t}} \left\| \Xi_{\mathbf{M}}^{\text{NN}}(\mathbf{x}_{j|\Gamma_t}) - \bar{\mathbf{M}}(\mathbf{x}_{j|\Gamma_t}) \right\| \quad (44)$$

where,  $\{\mathbf{x}_{1|\Omega}, \dots, \mathbf{x}_{N_c^{\Omega}|\Omega}\}$ ,  $\{\mathbf{x}_{1|\Gamma_u}, \dots, \mathbf{x}_{N_c^{\Gamma_u}|\Gamma_u}\}$ ,  $\{\mathbf{x}_{1|\Gamma_t}, \dots, \mathbf{x}_{N_c^{\Gamma_t}|\Gamma_t}\}$  are the collocation points over the domain  $\Omega$ , and along the boundaries  $\Gamma_u$  and  $\Gamma_t$ , respectively;  $\varphi \in \mathbb{R}^+$  is the penalty coefficient for imposing the biharmonic relation in Eq. 36. Additionally, data driven estimates of  $w(\mathbf{x})$ ,  $\mathbf{M}(\mathbf{x})$ , and  $\mathbf{Q}(\mathbf{x})$  at the collocation points across  $\Omega$  are used to define  $\Delta_{\mathcal{L}}(\mathbf{x}, \theta)$ .

$$\Delta_{\mathcal{L}}^w = \frac{1}{N_c^{\Omega}} \sum_{l=1}^{N_c^{\Omega}} \left\| \Xi_{\mathbf{w}}^{\text{NN}}(\mathbf{x}_{l|\Omega}) - \hat{w}(\mathbf{x}_{l|\Omega}) \right\| \quad (45)$$

$$\Delta_{\mathcal{L}}^M = \frac{1}{N_c^{\Omega}} \sum_{l=1}^{N_c^{\Omega}} \left\| \Xi_{\mathbf{M}}^{\text{NN}}(\mathbf{x}_{l|\Omega}) - \hat{\mathbf{M}}(\mathbf{x}_{l|\Omega}) \right\| \quad (46)$$

$$\Delta_{\mathcal{L}}^Q = \frac{1}{N_c^{\Omega}} \sum_{l=1}^{N_c^{\Omega}} \left\| \Xi_{\mathbf{Q}}^{\text{NN}}(\mathbf{x}_{l|\Omega}) - \hat{\mathbf{Q}}(\mathbf{x}_{l|\Omega}) \right\| \quad (47)$$

Here,  $\hat{w}(\mathbf{x}_{l|\Omega})$ ,  $\hat{\mathbf{M}}(\mathbf{x}_{l|\Omega})$ , and  $\hat{\mathbf{Q}}(\mathbf{x}_{l|\Omega})$  are obtained by means of analytical or high-fidelity numerical solutions. Note,  $\alpha_i = 1; \forall i = w, M, Q$  for data-driven enhancement coupled with physics-informed regression by forcing the PDE constraints in Eqs. 36-38. Whereas,  $\alpha_i = 0$  switches off the data-driven enhancement of accuracy of the NN approximations. The loss function in Eq. 41 can either be used for obtaining PINNs approximations of  $w(\mathbf{x})$ ,  $\mathbf{M}(\mathbf{x})$ , and  $\mathbf{Q}(\mathbf{x})$  (i.e., forward problem), or identification of model parameters  $\lambda$  and  $\mu$  (i.e., inverse problem).

### 5.3 Simply supported Kirchhoff-Love plate:

A simply supported rectangular plate of size  $(a \times b)$  under a sinusoidal load  $q(x, y) = q_0 \sin \frac{\pi x}{a} \sin \frac{\pi y}{b}$  is considered in Cartesian coordinates as shown in Fig. 7. Here,  $q_0$  is the intensity of the load at



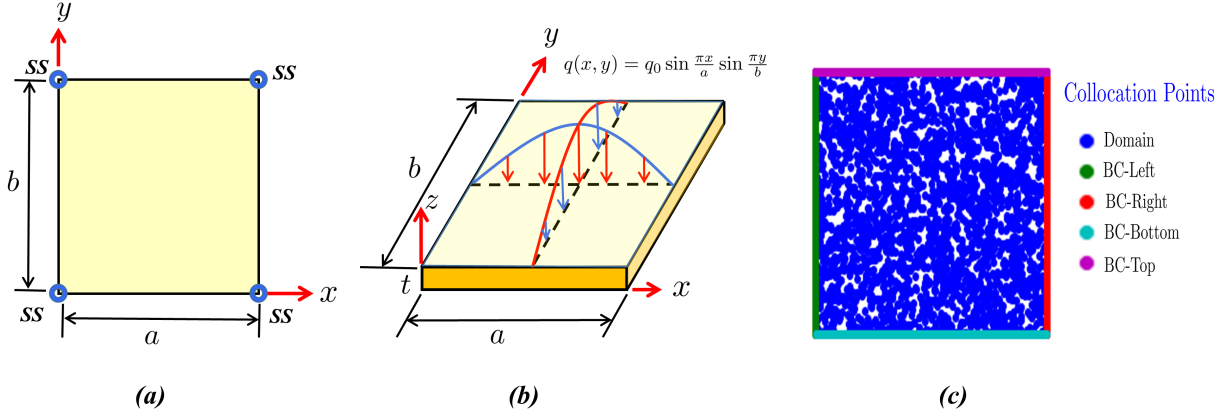


Figure 7: Benchmark problem setup for Kirchhoff-Love plate: (a, b) simply supported rectangular plate of  $a = 200$  cm and  $b = 300$  cm with thickness  $t = 1$  cm subjected to transverse sinusoidal loading of intensity  $q_0 = 9.806 \times 10^{-4}$  MPa; (b) distributions of total collocations points  $N_c = 10,000$  on the problem domain and various boundaries during PINNs training.

the center of the plate. The following boundary conditions are applied at the simply supported (SS) edges:

$$w = 0; \quad \frac{\partial^2 w}{\partial x^2} = 0 \quad \text{for } x = 0 \text{ and } x = a \quad (48)$$

$$w = 0; \quad \frac{\partial^2 w}{\partial y^2} = 0 \quad \text{for } y = 0 \text{ and } y = b \quad (49)$$

**5.3.1 Analytical solution:** Along with the governing equation in Eq. 36 and the boundary conditions in Eqs. 48- 49, the analytical solutions of  $w$  are obtained as:

$$w = \frac{q_0}{\pi^4 \left( \frac{1}{a^2} + \frac{1}{b^2} \right)^2} \sin \frac{\pi x}{a} \sin \frac{\pi y}{b} \quad (50)$$

Utilizing Eqs. 37-38, analytical solutions for the moments  $M_{xx}$ ,  $M_{yy}$ ,  $M_{xy}$  and the shearing forces,  $Q_{xx}$ ,  $Q_{yy}$  are obtained as:

$$M_{xx} = \frac{q_0}{\pi^2 \left( \frac{1}{a^2} + \frac{1}{b^2} \right)^2} \left( \frac{1}{a^2} + \frac{\nu}{b^2} \right) \sin \frac{\pi x}{a} \sin \frac{\pi y}{b} \quad (51)$$

$$M_{yy} = \frac{q_0}{\pi^2 \left( \frac{1}{a^2} + \frac{1}{b^2} \right)^2} \left( \frac{\nu}{a^2} + \frac{1}{b^2} \right) \sin \frac{\pi x}{a} \sin \frac{\pi y}{b} \quad (52)$$

$$M_{xy} = \frac{q_0(1-\nu)}{\pi^2 \left( \frac{1}{a^2} + \frac{1}{b^2} \right)^2} ab \left( \frac{\nu}{a^2} + \frac{1}{b^2} \right) \cos \frac{\pi x}{a} \cos \frac{\pi y}{b} \quad (53)$$

$$Q_{xx} = \frac{q_0}{\pi a \left( \frac{1}{a^2} + \frac{1}{b^2} \right)} \cos \frac{\pi x}{a} \sin \frac{\pi y}{b} \quad (54)$$

$$Q_{yy} = \frac{q_0}{\pi a \left( \frac{1}{a^2} + \frac{1}{b^2} \right)} \sin \frac{\pi x}{a} \sin \frac{\pi y}{b} \quad (55)$$

These analytical solutions,  $w(\mathbf{x})$ ,  $\mathbf{M}(\mathbf{x})$ , and  $\mathbf{Q}(\mathbf{x})$  have been utilized as  $\hat{w}(\mathbf{x}_{l|\Omega})$ ,  $\hat{\mathbf{M}}(\mathbf{x}_{l|\Omega})$ , and  $\hat{\mathbf{Q}}(\mathbf{x}_{l|\Omega})$  for data driven enhancement in Eqs. 45-47, respectively for the PINNs approximations of the field variables.

#### 5.4 PINNs solutions for the Biharmonic equation:

For the benchmark problem, a rectangular plate ( $a = 200$  cm,  $b = 300$  cm) with thickness  $t = 1$  cm is considered with the following material properties: Young's modulus of elasticity  $E = 202017.03$  MPa, Poisson's ratio  $\nu = 0.25$ , and flexural rigidity  $\mathcal{D} = 17957$  N-m. The sinusoidal load intensity  $q_0 = 9.806 \times 10^{-4}$  MPa is prescribed as shown in Fig. 7. A similar problem has been also solved in the recent work (Vahab et al., 2021). Unless otherwise stated, the total number of randomly distributed collocation points,  $N_c = 10,000$  is used during the training of the PINNs model. Additionally, a learning rate of 0.001, and a batch size of 50 were prescribed for optimal accuracy and faster convergence of the optimization scheme. For better accuracy during training, the Adam optimization scheme is employed with 1000 epochs. In the present study, three different activation functions were tested (see section 5.4.1).

In Fig. 8(a-f), the analytical solution for various fields including plate deflection  $w$ , moments  $M_{xx}$ ,  $M_{yy}$ ,  $M_{xy}$ , and shearing forces  $Q_{xx}$ , and  $Q_{yy}$  in Eqs. 50-55 are shown. Corresponding approximations from PINNs for various activation functions are shown in Fig. 8 (a-f) which illustrate the efficacy of the proposed model in terms of accuracy and robustness as excellent agreement with the analytical solutions is evident.

##### 5.4.1 Influence of the activation function:

The accuracy of the field variables and epoch evolution of the loss functions are explored for various activation functions for solving the fourth-order biharmonic PDE. To this end, three different activations, i.e., ReLU, sigmoid, and tanh are selected; the network used is defined by  $\mathcal{N} = 20$ ,  $L_n = 5$ . The corresponding results are depicted in Fig. 8 (g-l). Based on the results, all the activations perform well as the NN approximations are in good agreement with the analytical solutions both qualitatively and quantitatively. For further insight into the

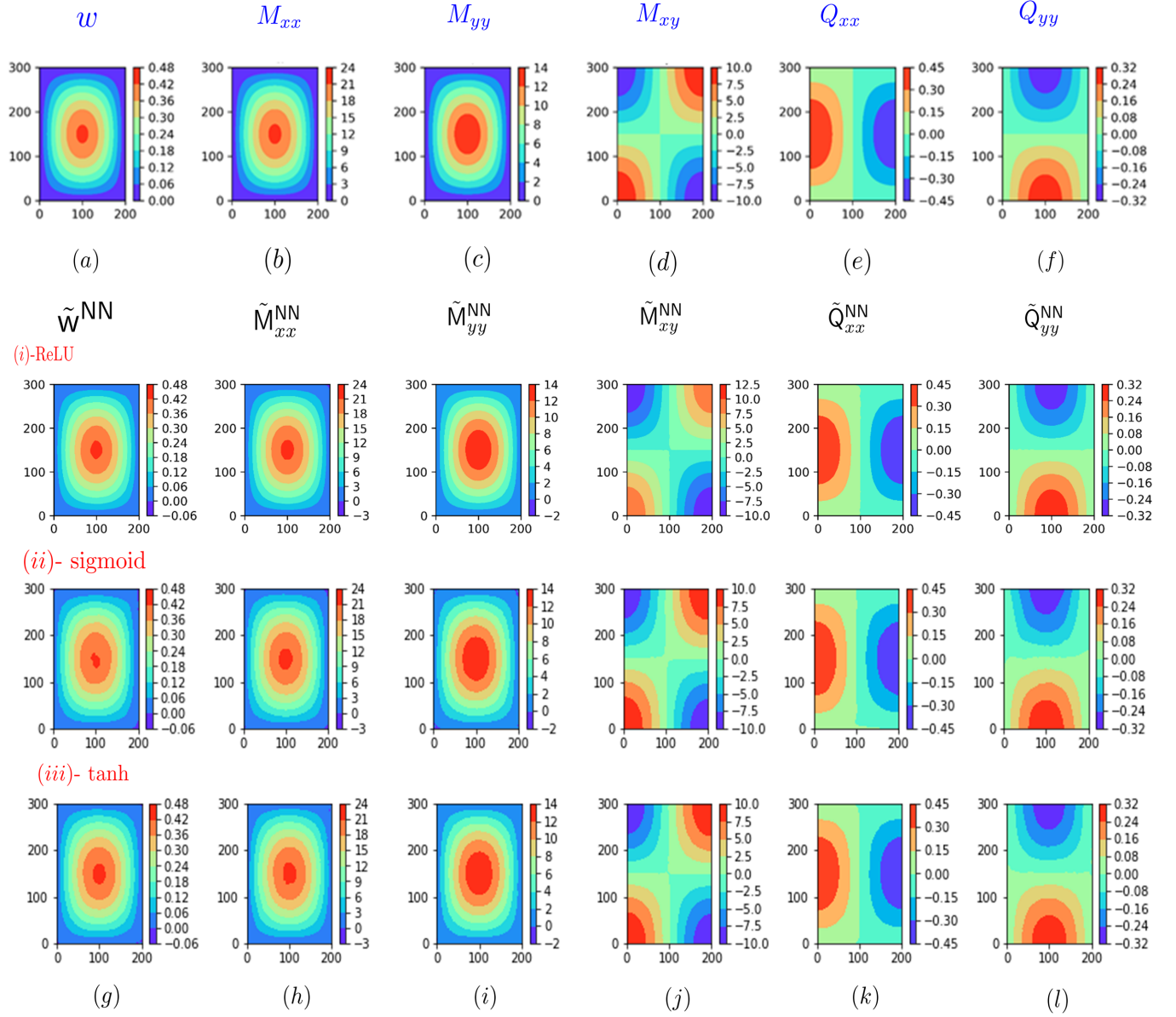


Figure 8: Solution of field variables obtained from (a-f) analytical solutions (left to right):  $w$ ,  $M_{xx}$ ,  $M_{yy}$ ,  $M_{xy}$ ,  $Q_{xx}$ , and  $Q_{yy}$ ; (g-l) proposed PINNs results (left to right):  $\tilde{w}^{NN}$ ,  $\tilde{M}_{xx}^{NN}$ ,  $\tilde{M}_{yy}^{NN}$ ,  $\tilde{M}_{xy}^{NN}$ ,  $\tilde{Q}_{xx}^{NN}$ , and  $\tilde{Q}_{yy}^{NN}$  for activation functions (i) ReLU, (ii) sigmoid, and (iii) tanh.

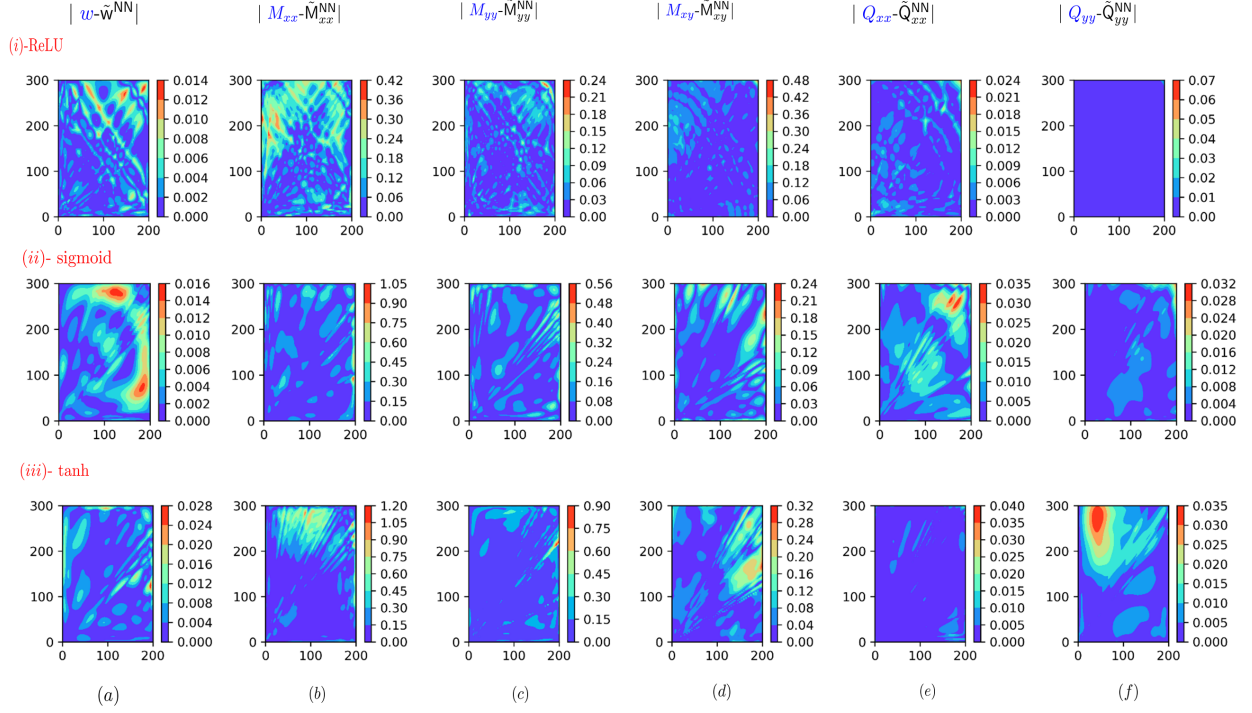


Figure 9: Absolute error of field variables between analytical solution and PINNs results (a)  $|w - \tilde{w}^{\text{NN}}|$ ; (b)  $|M_{xx} - \tilde{M}_{xx}^{\text{NN}}|$ ; (c)  $|M_{yy} - \tilde{M}_{yy}^{\text{NN}}|$ ; (d)  $|M_{xy} - \tilde{M}_{xy}^{\text{NN}}|$ ; (e)  $|Q_{xx} - \tilde{Q}_{xx}^{\text{NN}}|$ ; and (f)  $|Q_{yy} - \tilde{Q}_{yy}^{\text{NN}}|$  for activation functions (i) ReLU, (ii) sigmoid, and (iii) tanh.

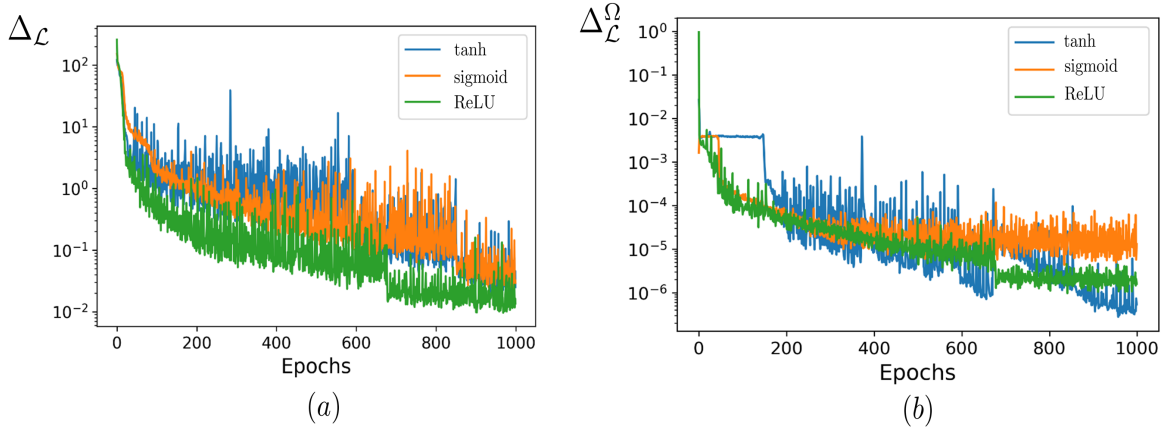


Figure 10: Comparison of (a) total loss  $\Delta_{\mathcal{L}}$ ; (b) constitutive loss  $\Delta_{\mathcal{L}}^{\Omega}$  during training for tanh, sigmoid and ReLU activation functions for network parameters  $\mathcal{N} = 20, L_n = 5$ .

Table 3: Influence of different activation functions on the final values of various loss components (in  $10^{-05}$ ) and training times  $t_{tr}$  in the proposed PINNs model for solving biharmonic PDE.

| Activation Function | $\Delta_{\mathcal{L}}^{\Omega}$ | $\Delta_{\mathcal{L}}^{\Gamma_t}$ | $\Delta_{\mathcal{L}}^{\Gamma_u}$ | $\Delta_{\mathcal{L}}^w$ | $\Delta_{\mathcal{L}}^M$ | $\Delta_{\mathcal{L}}^Q$ | $\Delta_{\mathcal{L}}$ | $t_{tr}$<br>(min) |
|---------------------|---------------------------------|-----------------------------------|-----------------------------------|--------------------------|--------------------------|--------------------------|------------------------|-------------------|
| ReLU                | 5.34                            | 132.31                            | 1672.91                           | 278.43                   | 498.76                   | 101.36                   | 2689.11                | 23.1              |
| Sigmoid             | 63.07                           | 980.67                            | 4601.60                           | 1707.50                  | 987.89                   | 117.56                   | 8458.29                | 25.8              |
| tanh                | 0.12                            | 7138.43                           | 9807.31                           | 6809.34                  | 397.89                   | 500.37                   | 24653.46               | 34.6              |

influence of an activation function on the accuracy of the solutions, the absolute error between the analytical solutions and the PINNs approximations for each field variable is compared for the solutions obtained with different activations in Fig. 9 (a–f). From the comparison, ReLU provides the least absolute error distributions in solving the Biharmonic equation for the simply supported plate. Although, the sigmoid activation provides the best result for  $|M_{xy} - \tilde{M}_{xy}^{NN}|$ , the absolute error for the rest of the fields is higher compared to the solutions obtained with ReLU. Because of the sinusoidal nature of the solution, it was expected that tanh activation might be specifically suitable for this problem. Surprisingly, tanh provides worse results compared to ReLU and sigmoid activations. This can be due to the complex nature of the solution space, where ReLU can provide better adaptability during training. Furthermore, in Fig. 10, the epoch evolution of the total loss  $\Delta_{\mathcal{L}}^{\Omega}$ , and constitutive loss  $\Delta_{\mathcal{L}}^{\Omega}$  is compared for different activation functions. For a particular epoch, ReLU performs better than the other two activations for  $\Delta_{\mathcal{L}}$ . For  $\Delta_{\mathcal{L}}^{\Omega}$ , tanh activation shows better convergence and the lowest loss value at the end of training due to the sinusoidal nature of the solution of the Biharmonic PDE. However, the fluctuations in the loss curve for tanh have a relatively higher variance compared to ReLU and sigmoid. As reported in Table 3, overall, performance in terms of various loss components at the end of training is superior for the ReLU activation for solving the Biharmonic PDE using the proposed PINNs framework. Additionally, the model with the ReLU activation requires the least training time  $t_{tr}$ , indicating better convergence and faster computation of the forward and backpropagation steps.

#### 5.4.2 Influence of network parameters:

As was found for the linear elasticity problem, PINNs solutions are sensitive to the NN architecture. Various parameters that influence the NN architectures, the number of neurons in each hidden layer  $\mathcal{N}$ , and the total number of hidden layers  $L_n$ , on the accuracy of the model and the efficiency of training the model have been explored herein. Because of its superior performance for the problem, ReLU is chosen as the activation function. Four different networks with combinations  $\mathcal{N} = 20, 40$ , and  $L_n = 5, 10$  were trained. Corresponding network parameters ( $n_p$ ), model training time ( $t_{tr}$ ), and values of different loss components at the end of training have been presented in Table. 4. The comparisons of the absolute error between the analytical solutions and the PINNs approximations for each field are shown in Fig. 11. Comparisons of the total loss  $\Delta_{\mathcal{L}}$ , the constitutive loss  $\Delta_{\mathcal{L}}^{\Omega}$  for various combinations of network parameters,  $\mathcal{N}$  and  $L_n$  are shown in Fig. 12.

Based on the comparisons shown in Fig. 11, increased network depth improves the accuracy of the PINNs approximations for all variables. Predictions by both networks with  $L_n = 10$  are superior compared to the analytical solutions for the chosen number of collocation points. On the other hand, an increase in the number of neurons in each layer increases model prediction variance which is reflected in the higher absolute error comparisons for  $\mathcal{N} = 20, 40$  and  $L_n = 10$ . Similar conclusions may be drawn based on Fig. 12 and Table. 4. The total and constitutive losses are minimum for  $\mathcal{N} = 40$  and  $L_n = 10$  at the end of training. However, the approximations by this model have higher variance. Expectedly, more complex models (higher  $L_n$ ), or with larger  $n_p$ , require longer training time  $t_{tr}$ . For the chosen number of collocation points,  $L_n = 10$  is optimal.

#### 5.4.3 Smart initialization of data-driven enhancement:

In this section, we explore the applicability of data-driven enhancement in the proposed PINNs framework to improve the accuracy of the solution. Initially, the network is trained with relatively low  $N_c = 10,000$ . The pre-trained model is then trained for the higher number of collocation datasets  $N_c = 15,000$  and  $N_c = 20,000$  to further improve the model accuracy.

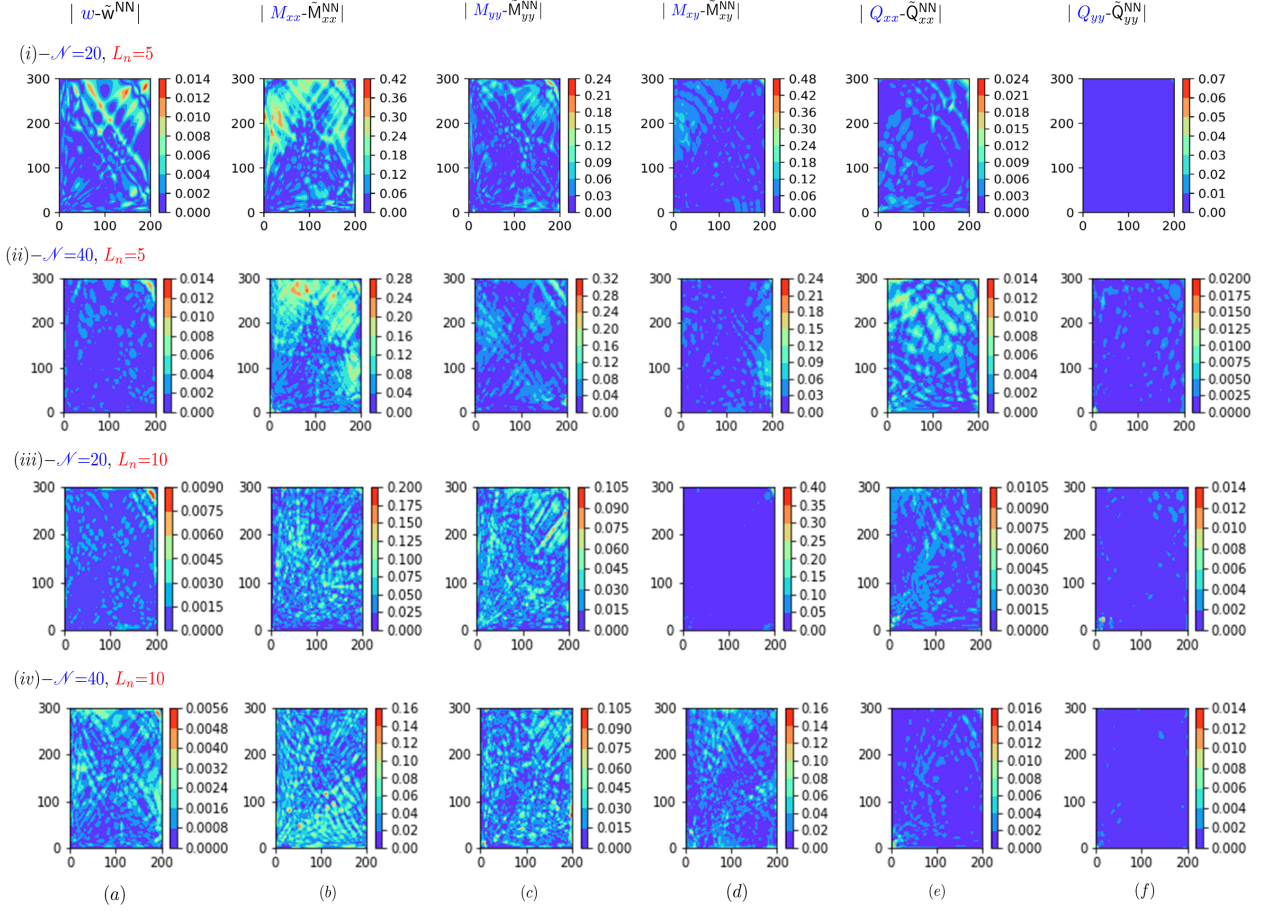


Figure 11: Absolute error of field variables between analytical solution and PINNs results (a)  $|w - \tilde{w}^{\text{NN}}|$ ; (b)  $|M_{xx} - \tilde{M}_{xx}^{\text{NN}}|$ ; (c)  $|M_{yy} - \tilde{M}_{yy}^{\text{NN}}|$ ; (d)  $|M_{xy} - \tilde{M}_{xy}^{\text{NN}}|$ ; (e)  $|Q_{xx} - \tilde{Q}_{xx}^{\text{NN}}|$ ; and (f)  $|Q_{yy} - \tilde{Q}_{yy}^{\text{NN}}|$  for various network parameters (i)  $\mathcal{N} = 20, L_n = 5$ , (ii)  $\mathcal{N} = 40, L_n = 5$ , (iii)  $\mathcal{N} = 20, L_n = 10$ , and (iv)  $\mathcal{N} = 40, L_n = 10$ .

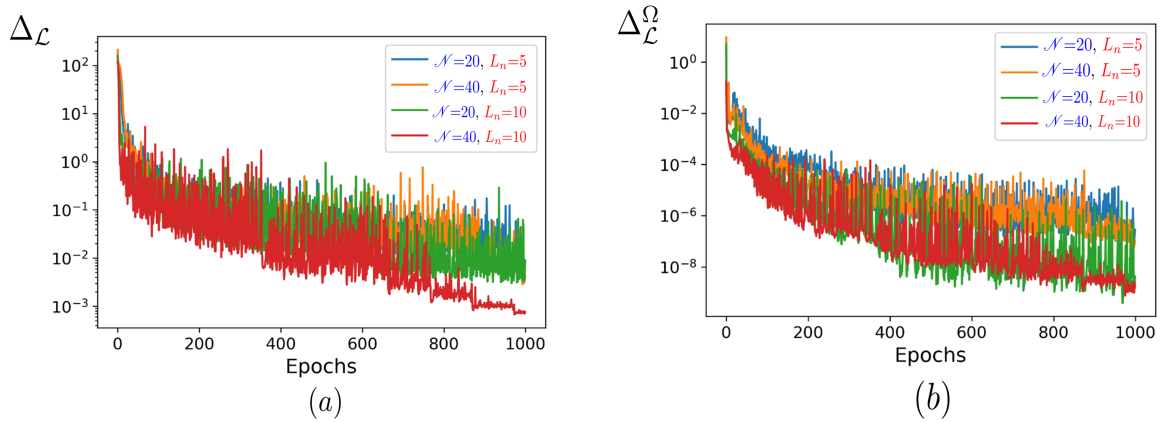


Figure 12: Comparison of (a) total loss  $\Delta_{\mathcal{L}}^{\Omega}$ ; (b) constitutive loss  $\Delta_{\mathcal{L}}^{\Omega}$  for various combinations of network parameters  $\mathcal{N}$  and  $L_n$  considering ReLU activation.

Table 4: Influence of network parameters  $\mathcal{N}$  and  $L_n$  on training times  $t_{tr}$  and final values of various loss components (in  $10^{-05}$ ) for tanh activation.

| Network identifier                   | $n_p$   | $t_{tr}$ (min) | $\Delta_{\mathcal{L}}^{\Omega}$ | $\Delta_{\mathcal{L}}^{\Gamma_u}$ | $\Delta_{\mathcal{L}}^{\Gamma_t}$ | $\Delta_{\mathcal{L}}^w$ | $\Delta_{\mathcal{L}}^M$ | $\Delta_{\mathcal{L}}^Q$ | $\Delta_{\mathcal{L}}$ |
|--------------------------------------|---------|----------------|---------------------------------|-----------------------------------|-----------------------------------|--------------------------|--------------------------|--------------------------|------------------------|
| N-1 ( $\mathcal{N} = 20, L_n = 5$ )  | 12,940  | 23.1           | 5.34                            | 132.31                            | 1672.91                           | 278.43                   | 498.76                   | 101.36                   | 2689.11                |
| N-2 ( $\mathcal{N} = 40, L_n = 5$ )  | 52,760  | 29.8           | 0.47                            | 35.13                             | 467.34                            | 128.38                   | 198.11                   | 40.29                    | 869.72                 |
| N-3 ( $\mathcal{N} = 20, L_n = 10$ ) | 32,056  | 31.7           | 0.07                            | 82.15                             | 86.84                             | 77.82                    | 298.01                   | 10.17                    | 555.06                 |
| N-4 ( $\mathcal{N} = 40, L_n = 10$ ) | 126,224 | 42.8           | 0.009                           | 0.67                              | 5.12                              | 4.21                     | 0.53                     | 0.17                     | 10.709                 |

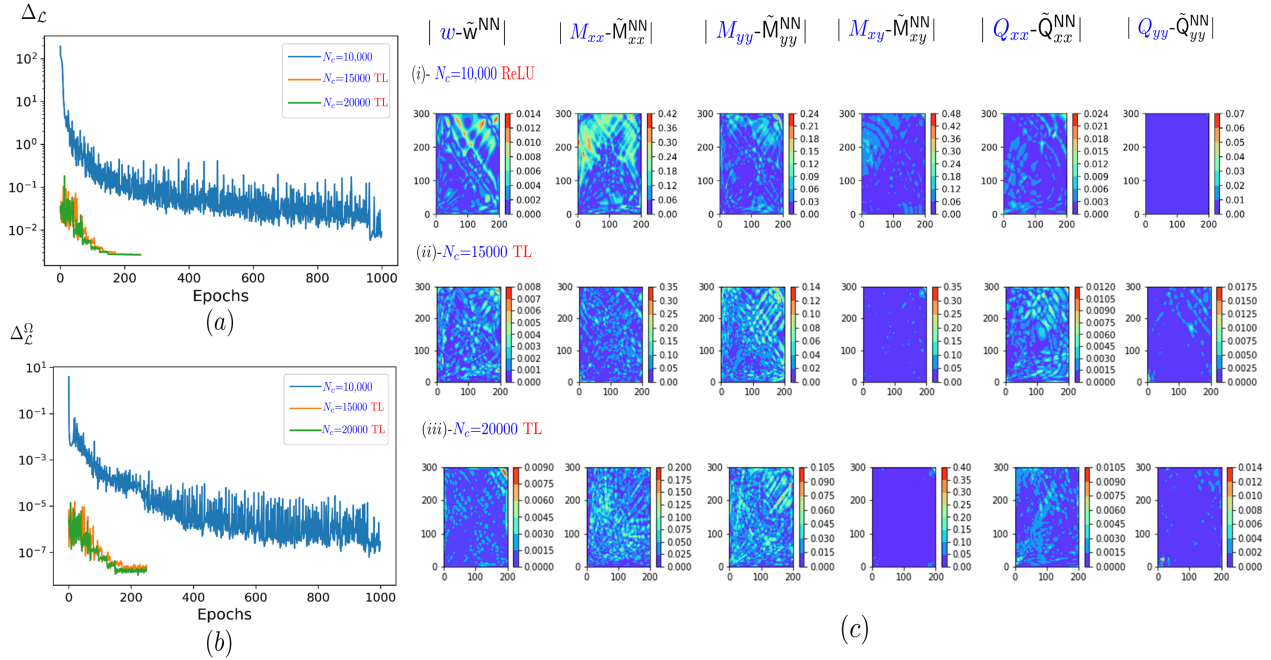


Figure 13: Influence of smart initialization of data-driven enhancement on (a) total loss  $\Delta_{\mathcal{L}}^{\Omega}$ ; (b) constitutive loss  $\Delta_{\mathcal{L}}^{\Omega}$  for increasing  $N_c$  considering ReLU activation; (c) Absolute error of field variables between analytical solution and PINNs results for (i)  $N_c = 10,000$ , (ii)  $N_c = 15,000$  TL, and  $N_c = 20,000$  TL.



Table 5: Network parameters, training time, and the component of loss for different smart initialization of data-driven enhancement models.

| Network identifier | $N_c$ | Epochs | $\Delta_{\mathcal{L}}^{\Omega}$ | $\Delta_{\mathcal{L}}^{\Gamma_t}$ | $\Delta_{\mathcal{L}}^{\Gamma_u}$ | $\Delta_{\mathcal{L}}^w$ | $\Delta_{\mathcal{L}}^M$ | $\Delta_{\mathcal{L}}^Q$ | $\Delta_{\mathcal{L}}$ | $t_{tr}$<br>(min) |
|--------------------|-------|--------|---------------------------------|-----------------------------------|-----------------------------------|--------------------------|--------------------------|--------------------------|------------------------|-------------------|
| N-1                | 10000 | 1000   | 5.34                            | 132.31                            | 1672.91                           | 278.43                   | 498.76                   | 101.36                   | 2689.11                | 23.1              |
| N-TL1              | 15000 | 250    | 0.025                           | 1.31                              | 17.34                             | 1.43                     | 13.11                    | 9.89                     | 43.11                  | 5.1               |
| N-TL2              | 20000 | 250    | 0.005                           | 0.71                              | 2.96                              | 2.01                     | 2.56                     | 0.87                     | 9.11                   | 7.2               |

The idea is to speed up the training by utilizing pre-trained weights; the initial states of the PINNs models in the later phases of training are not random anymore. The speed-up is reflected in Figs. 13-(a, b) when the convergence of the loss curves ( $\Delta_{\mathcal{L}}$  and  $\Delta_{\mathcal{L}}^{\Omega}$ ) for the pre-trained models corresponding to  $N_c = 15,000$  and  $N_c = 20,000$  are much improved compared to the first training phase with  $N_c = 10,000$ . In Fig. 13-(c), the absolute errors between the approximations and analytical solutions are shown which demonstrate significant improvement of the PINNs approximations with the increase in  $N_c$ . Additionally, parameters related to the efficiency of the network training processes with initialization of data-driven enhancement are reported in Tab. 5. The loss terms quickly reduce by orders of magnitude in the second training phase which indicates that for the considered network architecture,  $N_c = 15000$  is possibly optimal.

## 6. Discussions :

In the current study, a generalized PINNs framework for solving problems in linear continuum elasticity in the field of solid mechanics is presented. The fundamentals of the PINNs framework involve a construction of the loss function for physics-informed learning of the NNs through the embedding of the linear constraint during training. Following the PINNs philosophy to solve the linear elastic problem accurately, a multi-objective loss function has been formulated and implemented. The proposed multi-objective loss function consists of the residual of the governing PDE, various boundary conditions, and data-driven physical knowledge fitting terms. Additionally, weights corresponding to the terms in the loss function dictate

the emphasis on satisfying the specific loss terms. To demonstrate the efficacy of the framework, the Airy solution to an end-loaded cantilever beam and the Kirchhoff-Love plate theory governed by fourth-order Biharmonic PDE has been solved. The proposed PINNs framework is shown to accurately solve different fields in both problems. Parametric investigations on activation functions and network architectures highlight the scope of improvement in terms of solution accuracy and performance. Data-driven enhancement of the PINNs approximations using analytical solutions significantly boosts accuracy and speed only using minimal network parameters. Therefore, such an approach can be employed to enhance solution accuracy for complex PDEs. Additionally, the applicability of a smart initialization of data-driven enhancement learning-based approach quickening the training process and also improving model accuracy have been illustrated. Such an approach would be key in achieving computational efficiency beyond conventional computational methods for solving linear continuum elasticity. The proposed PINNs elasticity solvers utilize Tensorflow as the backend which can be easily deployed in CPU/ GPU clusters, whereas, conventional algorithms lack such adaptability. Thus, it opens new possibilities for solving complex elasticity problems that have remained unsolved by conventional numerical algorithms in the regime of continuum mechanics. It is however worth noting that exploitation of the computational advantages of the PINNs framework depends on various factors including the choice of the network architectures, hyperparameter tuning, sampling techniques (distribution) of collocation points, etc. It has been shown that appropriate combinations of such factors significantly improve the training process and the trained models.

In the present study, random sampling of the collocation points has been considered which is simple, yet powerful, that can lead to a significantly better reconstruction of the elastic fields. Importantly, this approach does not increase computational complexity, and it is easy to implement. However, in elastic/elastoplastic PDE problem which exhibits local behavior (e.g., in presence of sharp, or very localized, features) or problems with singularities the performance of PINNs may vary drastically with various sampling procedures ([Daw et al., 2022](#); [Leiteritz and Pflüger, 2021](#)). To overcome such an issue, a failure-informed adaptive enrichment strategy such as failure-informed PINNs (FI-PINNs) can be employed that adopts the failure probability as the posterior error indicator to generate new training points in the failure region ([Gao et al.,](#)

2022). Furthermore, the basic resampling scheme can be further improved with a gradient-based adaptive scheme to relocate the collocation points through a cosine-annealing to areas with higher loss gradient, without increasing the total number of points that demonstrated significant improvement under relatively fewer number of collocation points and sharper forcing function (Subramanian et al., 2022). In addition, the evolutionary sampling (Evo) method (Daw et al., 2022) that can incrementally accumulate collocation points in regions of high PDE residuals can be an efficient choice for solving various time-dependent PDEs with little to no computational overhead. Instead of using a random approach such as Latin Hypercube sampling, in the future, different deterministic and pseudo-random sampling strategies such as Sparse Grid sampling or Sobol Sequences can be employed to further improve the performance of the model.

Furthermore, it is critical to obtain the statics of saturation along different parts of the solution domain during the training of DNNs (Glorot and Bengio, 2010; Rakitianskaia and Engelbrecht, 2015b). The saturation occurs when the hidden units of a DNN predominantly output values close to the asymptotic ends of the activation function range which reduces the particular PINNs model to a binary state, thus limiting the overall information capacity of the NN (Rakitianskaia and Engelbrecht, 2015a; Bai et al., 2019). The saturated units can make gradient descent learning slow and inefficient due to small derivative values near the asymptotes which can hinder the training PINNs efficiently (Bai et al., 2019). Thus, in the future, NN saturation can be studied quantitatively in relation to the ability of NNs to learn, generalize, and the degree of regression accuracy. In addition, various weighting coefficients of the loss terms in Eq. 8 and implementation of second-order optimization techniques (Tan and Lim, 2019) can accelerate the training significantly. Based on the performance of the PINNs framework herein, further studies quantifying the computational gains of the PINNs approach compared to conventional numerical methods are in order. The proposed approach can be extended to the solution in various computational mechanics problems such as soil plasticity (Chen and Baladi, 1985; Bousshine et al., 2001), strain-gradient plasticity (Guha et al., 2013, 2014), composite modeling (Roy, 2021c) etc. Furthermore, the present model can be employed to predict microstructure evolution in Phase-field (PF) approach including various solid-solid phase transitions (PTs) (Levitas et al., 2013; Levitas and Roy, 2015; Roy, 2020c,a,b),

solid-solid PT via intermediate melting (Levitas and Roy, 2016; Roy, 2021a,f,e,d,b, 2022d), etc.

## 7. Conclusions :

Summarizing, the current work presents a deep learning framework based on the fundamentals of PINNs theory for the solution of linear elasticity problems in continuum mechanics. A multi-objective loss function is proposed for the linear elastic solid problems that include governing PDE, Dirichlet, and Neumann boundary conditions across randomly chosen collocation points in the problem domain. Multiple deep network models trained to predict different fields result in a more accurate representation. Traditional ML/ DL approaches that only rely on fitting a model that establishes complex, high-dimensional, non-linear relationships between the input features and outputs, are unable to incorporate rich information available through governing equations/ physics-based mathematical modeling of physical phenomena. Conventional computational techniques on the other hand rely completely on such physical information for prediction. The PINNs approach combines the benefits of the DL techniques in the extraction of complex relations from data with the advantages of the conventional numerical techniques for physical modeling. The proposed method may be extended to nonlinear elasticity, viscoplasticity, elastoplasticity, and various other mechanics and material science problems. The present work builds a solid foundation for new promising avenues for future work in machine learning applications in solid mechanics.

**Acknowledgements:** The support of the Aeronautical Research and Development Board (Grant No. DARO/08/1051450/M/I) is gratefully acknowledged.

**Competing interests:** The author declares no competing interests.

## References

- Arora, R., Kakkar, P., Dey, B., and Chakraborty, A. (2022). Physics-informed neural networks for modeling rate-and temperature-dependent plasticity. *arXiv preprint arXiv:2201.08363*.
- Atkin, R. J. and Fox, N. (2005). *An introduction to the theory of elasticity*. Courier Corporation.

- Bai, W., Zhou, Q., Li, T., and Li, H. (2019). Adaptive reinforcement learning neural network control for uncertain nonlinear system with input saturation. *IEEE transactions on cybernetics*, 50(8):3433–3443.
- Batra, R., Song, L., and Ramprasad, R. (2021). Emerging materials intelligence ecosystems propelled by machine learning. *Nature Reviews Materials*, 6(8):655–678.
- Baydin, A. G., Pearlmutter, B. A., Radul, A. A., and Siskind, J. M. (2018). Automatic differentiation in machine learning: a survey. *Journal of machine learning research*, 18.
- Bekar, A. C., Madenci, E., Haghghat, E., Waheed, U. b., and Alkhalifah, T. (2022). Solving the eikonal equation for compressional and shear waves in anisotropic media using peridynamic differential operator. *Geophysical Journal International*, 229(3):1942–1963.
- Bergen, K. J., Johnson, P. A., Maarten, V., and Beroza, G. C. (2019). Machine learning for data-driven discovery in solid earth geoscience. *Science*, 363(6433).
- Bilbao, I. and Bilbao, J. (2017). Overfitting problem and the over-training in the era of data: Particularly for artificial neural networks. In *2017 eighth international conference on intelligent computing and information systems (ICICIS)*, pages 173–177. IEEE.
- bin Waheed, U., Alkhalifah, T., Haghghat, E., and Song, C. (2022). A holistic approach to computing first-arrival traveltimes using neural networks. In *Advances in Subsurface Data Analytics*, pages 251–278. Elsevier.
- bin Waheed, U., Haghghat, E., Alkhalifah, T., Song, C., and Hao, Q. (2021). Pinneik: Eikonal solution using physics-informed neural networks. *Computers & Geosciences*, 155:104833.
- Bose, R. and Roy, A. (2022). Accurate deep learning sub-grid scale models for large eddy simulations. *Bulletin of the American Physical Society*.
- Bousshine, L., Chaaba, A., and De Saxce, G. (2001). Softening in stress–strain curve for drucker–prager non-associated plasticity. *International Journal of Plasticity*, 17(1):21–46.
- Bower, A. F. (2009). *Applied mechanics of solids*. CRC press.
- Boyd, J. P. (2001). *Chebyshev and Fourier spectral methods*. Courier Corporation.

- Brunton, S. L., Noack, B. R., and Koumoutsakos, P. (2020). Machine learning for fluid mechanics. *Annual Review of Fluid Mechanics*, 52:477–508.
- Butler, K. T., Davies, D. W., Cartwright, H., Isayev, O., and Walsh, A. (2018). Machine learning for molecular and materials science. *Nature*, 559(7715):547–555.
- Cai, S., Wang, Z., Wang, S., Perdikaris, P., and Karniadakis, G. E. (2021). Physics-informed neural networks for heat transfer problems. *Journal of Heat Transfer*, 143(6).
- Chandio, A., Gui, G., Kumar, T., Ullah, I., Ranjbarzadeh, R., Roy, A. M., Hussain, A., and Shen, Y. (2022). Precise single-stage detector. *arXiv preprint arXiv:2210.04252*.
- Chen, W.-F. and Baladi, G. Y. (1985). *Soil plasticity: theory and implementation*. Elsevier.
- Ching, T., Himmelstein, D. S., Beaulieu-Jones, B. K., Kalinin, A. A., Do, B. T., Way, G. P., Ferrero, E., Agapow, P.-M., Zietz, M., Hoffman, M. M., et al. (2018). Opportunities and obstacles for deep learning in biology and medicine. *Journal of The Royal Society Interface*, 15(141):20170387.
- Chollet, F. et al. (2015). keras.
- Dana, S. and Wheeler, M. F. (2020). A machine learning accelerated fe homogenization algorithm for elastic solids. *arXiv preprint arXiv:2003.11372*.
- Daw, A., Bu, J., Wang, S., Perdikaris, P., and Karpatne, A. (2022). Rethinking the importance of sampling in physics-informed neural networks. *arXiv preprint arXiv:2207.02338*.
- De Ryck, T., Jagtap, A. D., and Mishra, S. (2022). Error estimates for physics informed neural networks approximating the navier-stokes equations. *arXiv preprint arXiv:2203.09346*.
- DeVries, P. M., Viégas, F., Wattenberg, M., and Meade, B. J. (2018). Deep learning of aftershock patterns following large earthquakes. *Nature*, 560(7720):632–634.
- Du, Y. and Zaki, T. A. (2021). Evolutional deep neural network. *Phys. Rev. E*, 104:045303.
- Frankel, A., Tachida, K., and Jones, R. (2020). Prediction of the evolution of the stress field of polycrystals undergoing elastic-plastic deformation with a hybrid neural network model. *Machine Learning: Science and Technology*, 1(3):035005.

- Gao, Z., Yan, L., and Zhou, T. (2022). Failure-informed adaptive sampling for pinns. *arXiv preprint arXiv:2210.00279*.
- Glorot, X. and Bengio, Y. (2010). Understanding the difficulty of training deep feedforward neural networks. In *Proceedings of the thirteenth international conference on artificial intelligence and statistics*, pages 249–256. JMLR Workshop and Conference Proceedings.
- Glowacz, A. (2021). Fault diagnosis of electric impact drills using thermal imaging. *Measurement*, 171:108815.
- Glowacz, A. (2022). Thermographic fault diagnosis of shaft of bldc motor. *Sensors*, 22(21):8537.
- Goswami, S., Anitescu, C., Chakraborty, S., and Rabczuk, T. (2020). Transfer learning enhanced physics informed neural network for phase-field modeling of fracture. *Theoretical and Applied Fracture Mechanics*, 106:102447.
- Goswami, S., Yin, M., Yu, Y., and Karniadakis, G. E. (2022). A physics-informed variational deeponet for predicting crack path in quasi-brittle materials. *Computer Methods in Applied Mechanics and Engineering*, 391:114587.
- Guha, S., Sangal, S., and Basu, S. (2013). Finite element studies on indentation size effect using a higher order strain gradient theory. *International Journal of Solids and Structures*, 50(6):863–875.
- Guha, S., Sangal, S., and Basu, S. (2014). On the fracture of small samples under higher order strain gradient plasticity. *International Journal of Fracture*, 187(2):213–226.
- Guo, M. and Haghghat, E. (2020). An energy-based error bound of physics-informed neural network solutions in elasticity. *arXiv preprint arXiv:2010.09088*.
- Guo, X., Liu, X., Królczyk, G., Sulowicz, M., Glowacz, A., Gardoni, P., and Li, Z. (2022). Damage detection for conveyor belt surface based on conditional cycle generative adversarial network. *Sensors*, 22(9):3485.
- Haghghat, E., Amini, D., and Juanes, R. (2022). Physics-informed neural network simulation of multiphase poroelasticity using stress-split sequential training. *Computer Methods in Applied Mechanics and Engineering*, 397:115141.

- Haghighat, E., Bekar, A. C., Madenci, E., and Juanes, R. (2021a). A nonlocal physics-informed deep learning framework using the peridynamic differential operator. *Computer Methods in Applied Mechanics and Engineering*, 385:114012.
- Haghighat, E. and Juanes, R. (2021). Sciann: A keras/tensorflow wrapper for scientific computations and physics-informed deep learning using artificial neural networks. *Computer Methods in Applied Mechanics and Engineering*, 373:113552.
- Haghighat, E., Raissi, M., Moure, A., Gomez, H., and Juanes, R. (2020). A deep learning framework for solution and discovery in solid mechanics. *arXiv preprint arXiv:2003.02751*.
- Haghighat, E., Raissi, M., Moure, A., Gomez, H., and Juanes, R. (2021b). A physics-informed deep learning framework for inversion and surrogate modeling in solid mechanics. *Computer Methods in Applied Mechanics and Engineering*, 379:113741.
- Hu, Z., Jagtap, A. D., Karniadakis, G. E., and Kawaguchi, K. (2021). When do extended physics-informed neural networks (xpinns) improve generalization? *arXiv preprint arXiv:2109.09444*.
- Irfan, M., Iftikhar, M. A., Yasin, S., Draz, U., Ali, T., Hussain, S., Bukhari, S., Alwadie, A. S., Rahman, S., Glowacz, A., et al. (2021). Role of hybrid deep neural networks (hdnns), computed tomography, and chest x-rays for the detection of covid-19. *International Journal of Environmental Research and Public Health*, 18(6):3056.
- Jabbar, H. and Khan, R. Z. (2015). Methods to avoid over-fitting and under-fitting in supervised machine learning (comparative study). *Computer Science, Communication and Instrumentation Devices*, 70.
- Jagtap, A. D. and Karniadakis, G. E. (2021). Extended physics-informed neural networks (xpinns): A generalized space-time domain decomposition based deep learning framework for nonlinear partial differential equations. In *AAAI Spring Symposium: MLPS*.
- Jagtap, A. D., Kharazmi, E., and Karniadakis, G. E. (2020). Conservative physics-informed neural networks on discrete domains for conservation laws: Applications to forward and inverse problems. *Computer Methods in Applied Mechanics and Engineering*, 365:113028.



- Jagtap, A. D., Mao, Z., Adams, N., and Karniadakis, G. E. (2022). Physics-informed neural networks for inverse problems in supersonic flows. *arXiv preprint arXiv:2202.11821*.
- Jahanbakht, M., Xiang, W., and Azghadi, M. R. (2022). Sediment prediction in the great barrier reef using vision transformer with finite element analysis. *Neural Networks*, 152:311–321.
- Jamil, S., Abbas, M. S., and Roy, A. M. (2022). Distinguishing malicious drones using vision transformer. *AI*, 3(2):260–273.
- Jin, X., Cai, S., Li, H., and Karniadakis, G. E. (2021). Nsfnets (navier-stokes flow nets): Physics-informed neural networks for the incompressible navier-stokes equations. *Journal of Computational Physics*, 426:109951.
- Karniadakis, G. E., Kevrekidis, I. G., Lu, L., Perdikaris, P., Wang, S., and Yang, L. (2021). Physics-informed machine learning. *Nature Reviews Physics*, 3(6):422–440.
- Khan, W., Kumar, T., Cheng, Z., Raj, K., Roy, A. M., and Luo, B. (2022a). Sql and nosql databases software architectures performance analysis and assessments—a systematic literature review. *arXiv preprint arXiv:2209.06977*.
- Khan, W., Raj, K., Kumar, T., Roy, A. M., and Luo, B. (2022b). Introducing urdu digits dataset with demonstration of an efficient and robust noisy decoder-based pseudo example generator. *Symmetry*, 14(10):1976.
- Krishnapriyan, A., Gholami, A., Zhe, S., Kirby, R., and Mahoney, M. W. (2021). Characterizing possible failure modes in physics-informed neural networks. *Advances in Neural Information Processing Systems*, 34.
- Kutz, J. N. (2017). Deep learning in fluid dynamics. *Journal of Fluid Mechanics*, 814:1–4.
- Lagaris, I. E., Likas, A., and Fotiadis, D. I. (1998). Artificial neural networks for solving ordinary and partial differential equations. *IEEE transactions on neural networks*, 9(5):987–1000.
- LeCun, Y., Bengio, Y., and Hinton, G. (2015). Deep learning. *nature*, 521(7553):436–444.

- Leiteritz, R. and Pflüger, D. (2021). How to avoid trivial solutions in physics-informed neural networks. *arXiv preprint arXiv:2112.05620*.
- Levitas, V. I. and Roy, A. M. (2015). Multiphase phase field theory for temperature-and stress-induced phase transformations. *Physical Review B*, 91(17):174109.
- Levitas, V. I. and Roy, A. M. (2016). Multiphase phase field theory for temperature-induced phase transformations: Formulation and application to interfacial phases. *Acta Materialia*, 105:244–257.
- Levitas, V. I., Roy, A. M., and Preston, D. L. (2013). Multiple twinning and variant-variant transformations in martensite: phase-field approach. *Physical Review B*, 88(5):054113.
- Ling, J., Kurzawski, A., and Templeton, J. (2016). Reynolds averaged turbulence modelling using deep neural networks with embedded invariance. *Journal of Fluid Mechanics*, 807:155–166.
- Lou, Q., Meng, X., and Karniadakis, G. E. (2021). Physics-informed neural networks for solving forward and inverse flow problems via the boltzmann-bgk formulation. *Journal of Computational Physics*, 447:110676.
- Lurie, A. I. (2010). *Theory of elasticity*. Springer Science & Business Media.
- Määtä, J., Bazaliy, V., Kimari, J., Djurabekova, F., Nordlund, K., and Roos, T. (2021). Gradient-based training and pruning of radial basis function networks with an application in materials physics. *Neural Networks*, 133:123–131.
- Marsden, J. E. and Hughes, T. J. (1994). *Mathematical foundations of elasticity*. Courier Corporation.
- McClenny, L. and Braga-Neto, U. (2020). Self-adaptive physics-informed neural networks using a soft attention mechanism. *arXiv preprint arXiv:2009.04544*.
- Racca, A. and Magri, L. (2021). Robust optimization and validation of echo state networks for learning chaotic dynamics. *Neural Networks*, 142:252–268.

- Raissi, M. and Karniadakis, G. E. (2018). Hidden physics models: Machine learning of nonlinear partial differential equations. *Journal of Computational Physics*, 357:125–141.
- Raissi, M., Perdikaris, P., and Karniadakis, G. E. (2019). Physics-informed neural networks: A deep learning framework for solving forward and inverse problems involving nonlinear partial differential equations. *Journal of Computational Physics*, 378:686–707.
- Raissi, M., Yazdani, A., and Karniadakis, G. E. (2020). Hidden fluid mechanics: Learning velocity and pressure fields from flow visualizations. *Science*, 367(6481):1026–1030.
- Rakitianskaia, A. and Engelbrecht, A. (2015a). Measuring saturation in neural networks. In *2015 IEEE symposium series on computational intelligence*, pages 1423–1430. IEEE.
- Rakitianskaia, A. and Engelbrecht, A. (2015b). Saturation in pso neural network training: Good or evil? In *2015 IEEE Congress on Evolutionary Computation (CEC)*, pages 125–132. IEEE.
- Ramprasad, R., Batra, R., Pilania, G., Mannodi-Kanakkithodi, A., and Kim, C. (2017). Machine learning in materials informatics: recent applications and prospects. *npj Computational Materials*, 3(1):1–13.
- Rao, C., Sun, H., and Liu, Y. (2021). Physics-informed deep learning for computational elastodynamics without labeled data. *Journal of Engineering Mechanics*, 147(8):04021043.
- Rawat, W. and Wang, Z. (2017). Deep convolutional neural networks for image classification: A comprehensive review. *Neural computation*, 29(9):2352–2449.
- Reddy, J. N. (2006). *Theory and analysis of elastic plates and shells*. CRC press.
- Rezaei, S., Harandi, A., Moeineddin, A., Xu, B.-X., and Reese, S. (2022). A mixed formulation for physics-informed neural networks as a potential solver for engineering problems in heterogeneous domains: comparison with finite element method. *Computer Methods in Applied Mechanics and Engineering*, 401:115616.
- Roy, A. M. (2020a). Effects of interfacial stress in phase field approach for martensitic phase transformation in nial shape memory alloys. *Applied Physics A*, 126(7):1–12.

- Roy, A. M. (2020b). Evolution of martensitic nanostructure in nial alloys: tip splitting and bending. *Material Science Research India (Online)*, 17(special 1):03–06.
- Roy, A. M. (2020c). Influence of interfacial stress on microstructural evolution in nial alloys. *JETP Letters*, 112(3):173–179.
- Roy, A. M. (2021a). Barrierless melt nucleation at solid-solid interface in energetic nitramine octahydro-1, 3, 5, 7-tetranitro-1, 3, 5, 7-tetrazocine. *Materialia*, 15:101000.
- Roy, A. M. (2021b). Energetics and kinematics of undercooled nonequilibrium interfacial molten layer in cyclotetramethylene-tetranitramine crystal. *Physica B: Condensed Matter*, 615:412986.
- Roy, A. M. (2021c). Finite element framework for efficient design of three dimensional multi-component composite helicopter rotor blade system. *Eng*, 2(1):69–79.
- Roy, A. M. (2021d). Formation and stability of nanosized, undercooled propagating intermediate melt during  $\beta \rightarrow \delta$  phase transformation in hmx nanocrystal. *Europhysics Letters*, 133(5):56001.
- Roy, A. M. (2021e). Influence of nanoscale parameters on solid–solid phase transformation in octogen crystal: Multiple solution and temperature effect. *JETP Letters*, 113(4):265–272.
- Roy, A. M. (2021f). Multiphase phase-field approach for solid–solid phase transformations via propagating interfacial phase in hmx. *Journal of Applied Physics*, 129(2):025103.
- Roy, A. M. (2022a). Adaptive transfer learning-based multiscale feature fused deep convolutional neural network for eeg mi multiclassification in brain–computer interface. *Engineering Applications of Artificial Intelligence*, 116:105347.
- Roy, A. M. (2022b). An efficient multi-scale CNN model with intrinsic feature integration for motor imagery EEG subject classification in brain-machine interfaces. *Biomedical Signal Processing and Control*, 74:103496.
- Roy, A. M. (2022c). A multi-scale fusion cnn model based on adaptive transfer learning for multi-class mi-classification in bci system. *BioRxiv*.

- Roy, A. M. (2022d). Multiphase phase-field approach for virtual melting: a brief review. *Roy AM Multiphase Phase-Field Approach for Virtual Melting: A Brief Review. Mat. Sci. Res. India*, 18(2).
- Roy, A. M. and Bhaduri, J. (2021). A deep learning enabled multi-class plant disease detection model based on computer vision. *AI*, 2(3):413–428.
- Roy, A. M. and Bhaduri, J. (2022). Real-time growth stage detection model for high degree of occultation using densenet-fused YOLOv4. *Computers and Electronics in Agriculture*, 193:106694.
- Roy, A. M., Bhaduri, J., Kumar, T., and Raj, K. (2022a). A computer vision-based object localization model for endangered wildlife detection. *Ecological Economics, Forthcoming*.
- Roy, A. M., Bhaduri, J., Kumar, T., and Raj, K. (2022b). Wildelect-yolo: An efficient and robust computer vision-based accurate object localization model for automated endangered wildlife detection. *Ecological Informatics*, page 101919.
- Roy, A. M., Bose, R., and Bhaduri, J. (2022c). A fast accurate fine-grain object detection model based on YOLOv4 deep neural network. *Neural Computing and Applications*, pages 1–27.
- Roy, A. M. and Guha, S. (2022). Elastoplastic physics-informed deep learning approach for j2 plasticity. *Available at SSRN 4332254*.
- Saha, P., Dash, S., and Mukhopadhyay, S. (2021). Physics-incorporated convolutional recurrent neural networks for source identification and forecasting of dynamical systems. *Neural Networks*, 144:359–371.
- Samaniego, E., Anitescu, C., Goswami, S., Nguyen-Thanh, V. M., Guo, H., Hamdia, K., Zhuang, X., and Rabczuk, T. (2020). An energy approach to the solution of partial differential equations in computational mechanics via machine learning: Concepts, implementation and applications. *Computer Methods in Applied Mechanics and Engineering*, 362:112790.
- Sengupta, T. (2013). *High accuracy computing methods: fluid flows and wave phenomena*. Cambridge University Press.

- Shukla, K., Jagtap, A. D., Blackshire, J. L., Sparkman, D., and Karniadakis, G. E. (2021). A physics-informed neural network for quantifying the microstructural properties of polycrystalline nickel using ultrasound data: A promising approach for solving inverse problems. *IEEE Signal Processing Magazine*, 39(1):68–77.
- Singh, A., Raj, K., Kumar, T., Verma, S., and Roy, A. M. (2023a). Deep learning-based cost-effective and responsive robot for autism treatment. *Drones*, 7(2):81.
- Singh, A., Ranjbarzadeh, R., Raj, K., Kumar, T., and Roy, A. M. (2023b). Understanding eeg signals for subject-wise definition of armoni activities. *arXiv preprint arXiv:2301.00948*.
- Sirignano, J. and Spiliopoulos, K. (2018). Dgm: A deep learning algorithm for solving partial differential equations. *Journal of computational physics*, 375:1339–1364.
- Subramanian, S., Kirby, R. M., Mahoney, M. W., and Gholami, A. (2022). Adaptive self-supervision algorithms for physics-informed neural networks. *arXiv preprint arXiv:2207.04084*.
- Sun, L., Gao, H., Pan, S., and Wang, J.-X. (2020). Surrogate modeling for fluid flows based on physics-constrained deep learning without simulation data. *Computer Methods in Applied Mechanics and Engineering*, 361:112732.
- Szilard, R. and Nash, W. (1974). Theory and analysis of plates, classical and numerical methods.
- Tan, H. H. and Lim, K. H. (2019). Review of second-order optimization techniques in artificial neural networks backpropagation. In *IOP conference series: materials science and engineering*, volume 495, page 012003. IOP Publishing.
- Tartakovsky, A. M., Marrero, C. O., Perdikaris, P., Tartakovsky, G. D., and Barajas-Solano, D. (2018). Learning parameters and constitutive relationships with physics informed deep neural networks. *arXiv preprint arXiv:1808.03398*.
- Timoshenko, S. (1970). *Theory of elastic stability 2e*. Tata McGraw-Hill Education.
- Timoshenko, S. and Woinowsky-Krieger, S. (1959). Theory of plates and shells.

- Vahab, M., Haghghat, E., Khaleghi, M., and Khalili, N. (2021). A physics-informed neural network approach to solution and identification of biharmonic equations of elasticity. *Journal of Engineering Mechanics*, 148(2):04021154.
- von Rueden, L., Mayer, S., Beckh, K., Georgiev, B., Giesselbach, S., Heese, R., Kirsch, B., Pfrommer, J., Pick, A., Ramamurthy, R., et al. (2019). Informed machine learning—a taxonomy and survey of integrating knowledge into learning systems. *arXiv preprint arXiv:1903.12394*.
- Voulodimos, A., Doulamis, N., Doulamis, A., and Protopapadakis, E. (2018). Deep learning for computer vision: A brief review. *Computational intelligence and neuroscience*, 2018.
- Waheed, U., Haghghat, E., Alkhalifah, T., Song, C., and Hao, Q. (2020). Eikonal solution using physics-informed neural networks. In *EAGE 2020 Annual Conference & Exhibition Online*, volume 2020, pages 1–5. European Association of Geoscientists & Engineers.
- Xu, K., Huang, D. Z., and Darve, E. (2021). Learning constitutive relations using symmetric positive definite neural networks. *Journal of Computational Physics*, 428:110072.
- Zhang, E., Dao, M., Karniadakis, G. E., and Suresh, S. (2022). Analyses of internal structures and defects in materials using physics-informed neural networks. *Science advances*, 8(7):eabk0644.
- Zhang, E., Yin, M., and Karniadakis, G. E. (2020). Physics-informed neural networks for non-homogeneous material identification in elasticity imaging. *arXiv preprint arXiv:2009.04525*.
- Zhao, Z.-Q., Zheng, P., Xu, S.-t., and Wu, X. (2019). Object detection with deep learning: A review. *IEEE transactions on neural networks and learning systems*, 30(11):3212–3232.
- Zhu, Q., Liu, Z., and Yan, J. (2021). Machine learning for metal additive manufacturing: predicting temperature and melt pool fluid dynamics using physics-informed neural networks. *Computational Mechanics*, 67(2):619–635.
- Zienkiewicz, O. C. and Taylor, R. L. (2005). *The finite element method for solid and structural mechanics*. Elsevier.